LITHOS 458–459 (2023) 107337

Contents lists available at ScienceDirect

LITHOS

journal homepage: www.elsevier.com/locate/lithos

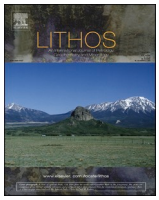

Extensive oxidizing events recorded by peridotite mantle xenoliths from the Hyblean Plateau: Evidence from combined measurements of ferric iron in spinel with noble gases and fluid inclusions chemistry in olivine

G. Marras [a,*], V. Stagno [a], G.B. Andreozzi [a,b], A. Caracausi [c,d], V. Cerantola [e,f], M.L. Frezzotti [e], M. Zacchigna [g], C. Perinelli [a]

[a] Dipartimento di Scienze della Terra, Sapienza Università di Roma, Roma, Italy
[b] Consiglio Nazionale delle Ricerche, Istituto di Geologia Ambientale e Geoingegneria, Sede Secondaria di Roma, c/o Dipartimento di Scienze della Terra, Sapienza Università di Roma, P.le A. Moro 5, Rome, Italy
[c] Istituto Nazionale di Geofisica e Vulcanologia (INGV), Sezione di Palermo, Via Ugo La Malfa 153, 90146 Palermo, Italy
[d] Departamento de Geología, Universidad de Salamanca, 37008 Salamanca, Spain
[e] Dipartimento di Scienze dell'Ambiente e della Terra, Università di Milano Bicocca, Piazza della Scienza 4, 20126 Milano, Italy
[f] European Synchrotron Radiation Facility, Grenoble, France
[g] IOM-CNR Laboratorio TASC, Area Science Park, 34012 Trieste, Italy

ARTICLE INFO

Keywords:
Hyblean craton
Redox state
Mössbauer spectroscopy
Noble gases
Raman
Abyssal peridotites

ABSTRACT

The study of the oxidation state of lithospheric mantle-derived rocks allows modelling the deep cycle of volatiles (e.g., C, H, O, N and S) in the Earth's interior, which in turn plays a role in magma genesis, metasomatism and volcanic degassing. At the oxygen fugacity (i.e., fO_2) recorded by residual abyssal peridotites, volatile elements like carbon are predicted to be in the immobile form of graphite. However, the compilation of the redox state of worldwide-distributed continental xenoliths shows evidence of their oxidation and refertilization through time by deeply formed subduction-related metasomatic fluids. The analyses of fluid inclusions in mantle-derived minerals like olivine (or pyroxenes) represent a snapshot of the volatile circulation in depth, whose noble gases signature (He, Ar, Ne) is used to identify their possible source. This study aims to reconstruct the origin of mantle metasomatism underneath the Hyblean Plateau (Sicily, Italy) and its redox history through the investigation of spinel-peridotite nodules, combining fO_2 estimates with noble gases and fluid inclusions chemistry from hand-picked olivine grains. We analyzed eight mantle xenoliths classified as spinel lherzolites and spinel harzburgites from the Valle Guffari (Hyblean Plateau, Sicily). The calculated $\log fO_2$ is higher than that of most cratonic xenoliths worldwide ranging between 0.28 and 1.27 log units above to the fayalite-magnetite-quartz (FMQ) reference buffer. Micro-Raman measurements on olivine grains with dendritic trails of (metasomatic) fluid inclusions reveal an assemblage made of Mg-Ca carbonates ± sulfide ± elemental sulfur ± CO_2 in the most reduced sample, and Mg-Ca carbonates ± sulfates ± CO_2 in the most oxidized sample, the latter associated with a silicate glass and (secondary) hydrous phases. Both assemblages are taken as evidence of the product of crystallization of deeply originated volatile-bearing silicate melts. Analyses of He, Ar, and Ne in olivine grains confirm the evidence of a mantle source reworked by metasomatic processes. Our data suggest that an initially residual Hyblean lithospheric mantle was affected by extensive oxidizing events at several depths caused by the interaction with slab-derived CO_2-rich silicate metasomatic liquids.

1. Introduction

Petrographic, petrological and geochemical investigations of mantle rocks are of primary importance for reconstructing the geodynamic and chemical evolution of the Earth's interior, the deep volatile cycle and rock-melt interaction. The chemical composition of coexisting rock-forming minerals in peridotites has allowed retrieving their equilibration pressure (P), temperature (T), and oxygen fugacity (fO_2) conditions,

* Corresponding author.
E-mail address: giulia.marras@uniroma1.it (G. Marras).

https://doi.org/10.1016/j.lithos.2023.107337
Received 31 August 2022; Received in revised form 16 August 2023; Accepted 22 August 2023
Available online 24 August 2023

often reported in comparative studies with the aim of providing an overview of the mantle redox state with respect to local geological settings (Frost and McCammon, 2008) and its effect on the formation of volatile-bearing magmas (Stagno, 2019). On the other hand, the investigation of mantle rocks at the micrometer-scale allows expanding our knowledge by looking at trapped inclusions, either minerals or fluids, that might reveal intermittent volatile influx along with the heating/cooling history of the rocky mantle. Previous studies consisting of petrographic, major and trace elements, noble gases, fluid inclusions, and C isotopes analyses of ultramafic xenoliths from the Hyblean Miocene diatremes (Sicily, Italy) showed a metasomatized upper mantle (depths within the spinel-peridotite stability field) likely due to the interaction with CO_2-rich metasomatic fluids (Correale et al., 2012, 2015; Perinelli et al., 2008; Sapienza et al., 2005; Sapienza and Scribano, 2000; Scribano et al., 2009). More in detail, according to petrographic observations, major and trace element composition of pyroxenes and glass veins, the last two metasomatic events recorded by the peridotites involved the reaction of the Hyblean upper mantle with 1) an alkaline silicate melt with a chemical composition similar to those melts that carried the xenoliths to the surface during the Miocene magmatic event, and 2) a volatile-free hawaiitic melt (Perinelli et al., 2008). Noble gases analyses (i.e., He, Ar, Ne) in olivines and clinopyroxenes of peridotitic and pyroxenitic nodules provided evidence of isotopic heterogeneity in the Hyblean mantle as consequence of the interaction between a residual high μ (HIMU)-like peridotitic mantle (where the parameter μ describes the $^{238}U/^{204}Pb$ ratio of an Earth reservoir) and pyroxenitic melts characterized by a depleted mantle (DM) end-member fingerprint (Correale et al., 2012) that, moving towards the surface, refertilized the upper portions of the mantle. Furthermore, Sapienza et al. (2005) argued that pure CO_2 fluid inclusions entrapped at shallow mantle depths (27–35 km) originated from a mid-ocean ridge basalt (MORB)-type source as suggested by $^3He/^4He$ values of 7.3 ± 0.3 Ra (where Ra is the air $^3He/^4He$ ratio of 1.38×10^{-6}). A subsequent detailed study of the C-noble gases systematics indicated that the Hyblean mantle was contaminated by a C-crustal component with an organic and sedimentary origin (Correale et al., 2015). These previous geochemical observations suggest the occurrence of a peridotitic mantle likely oxidized by metasomatic processes not necessarily related to one another. Such metasomatism resulted in $\log fO_2$ (normalized to the FMQ buffer) ranging between 0.15 and 1.61 log units as determined by Perinelli et al. (2008) who used microprobe data to calculate the Fe^{3+} content of spinel. Further, an accurate study of the inclusions in minerals like olivine can be used to retrieve the composition of the pristine oxidizing agent and its effect on the local fO_2.

To date, no studies exist that combine oxy-thermobarometric estimates for the Hyblean spinel peridotites along with their noble gases measurements and a detailed investigation of fluid inclusions in minerals. Such an approach provides further insight into the petrological processes triggered by the late Tertiary collision between the northern edge of the African foreland with the southern edge of the Eurasian plate. In this study, we first measured the ferric iron content of spinels of peridotitic xenoliths from the Hyblean tuff-breccia pipe of Valle Guffari by both conventional and in situ synchrotron Mössbauer spectroscopy. Hence, we determined the representative local mantle redox state by applying the spinel-bearing peridotite oxy-thermobarometer by Ballhaus et al. (1991) and then, we integrated these results with an accurate investigation of the inclusions in olivine by micro-Raman, Fourier transform infrared (FTIR) and noble gases isotopic signature. The results are discussed in light of previous studies conducted on xenoliths from the same area and compared with similar integrated data available in the most recent literature.

Table 1
Modal composition of Valle Guffari spinel peridotites expressed as percentage in volume of olivine, orthopyroxene, clinopyroxene and spinel, and relative rock classification according to Streckeisen (1974).

	Rock	Ol	Opx	Cpx	Spl
VG14	Lherzolite	64	26.6	8.4	1.0
VG21	Lherzolite	62	28.1	8.7	1.2
VG23	Lherzolite	65	25.5	8.4	1.1
VG24	Lherzolite	62.2	27.8	9.1	0.9
VG29	Harzburgite	64.5	30	4.6	0.9
VG34	Lherzolite	60.3	28.7	9.9	1.1
VG36	Harzburgite	76.9	19.4	3.2	0.5
VG40	Lherzolite	58.5	27.5	10.2	3.8

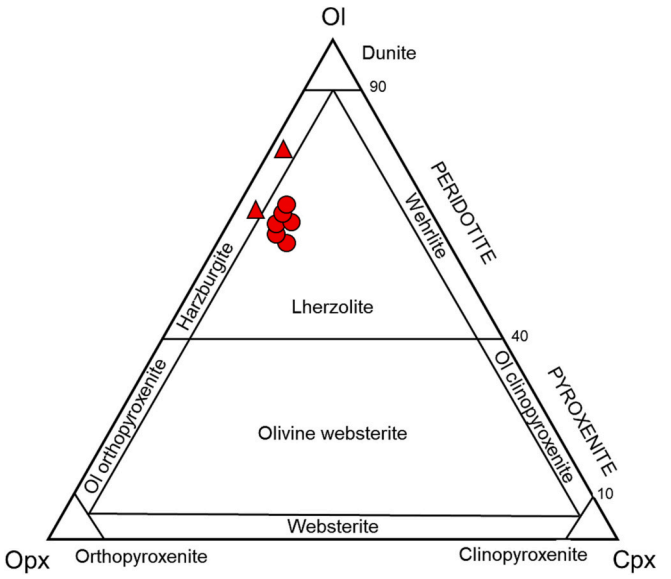

Fig. 1. Classification of Valle Guffari xenoliths according to the ultramafic rocks diagram (Streckeisen, 1974).

2. Materials and methods

2.1. Geological setting and mineralogy of the selected xenoliths

The Hyblean Plateau consists of a 12-km thick Meso-Cenozoic carbonate sequence and Neogene–Quaternary clasts intercalated by several levels of basic volcanic rocks that testify a discontinuous volcanic activity from the Upper Triassic to Plio-Pleistocene (Cristofolini, 1966). Three main magmatic episodes are known in the area: Cretaceous alkali basalts, Miocene alkali-basaltic lavas and tuff-breccia pipes, and Plio-Pleistocene lava flows whose compositions span from tholeiitic to alkaline (ocean-island basalt (OIB)-like; Beccaluva et al., 1998; Trua et al., 1998). Many mantle- and crust-derived xenoliths were found in Miocene diatremes and Quaternary nephelinite lava flows. A valuable cross-section of the area of interest has been recently proposed by Scribano and Carbone (2020), providing evidence of the geochemical and petrological basis of the involvement of deeper rocks represented by the peridotitic lithosphere, gradually followed upwards by moderately serpentinized peridotite rocks both cut by injections of garnet/spinel pyroxenites. The uppermost portion is represented by rocks representative of a fully serpentinized spreading ridge cut by gabbros and mafic products with MORB affinity. Petrography and mineral chemistry of the eight selected xenoliths were discussed in detail by Perinelli et al. (2008) and, according to the P estimates (0.85–1.30 GPa), these would be constituents of those moderately serpentized peridotites at depths of 20–30 km (see Fig. 9 in Scribano and Carbone, 2020). Because this manuscript deals with hand-picked minerals, rather than the whole

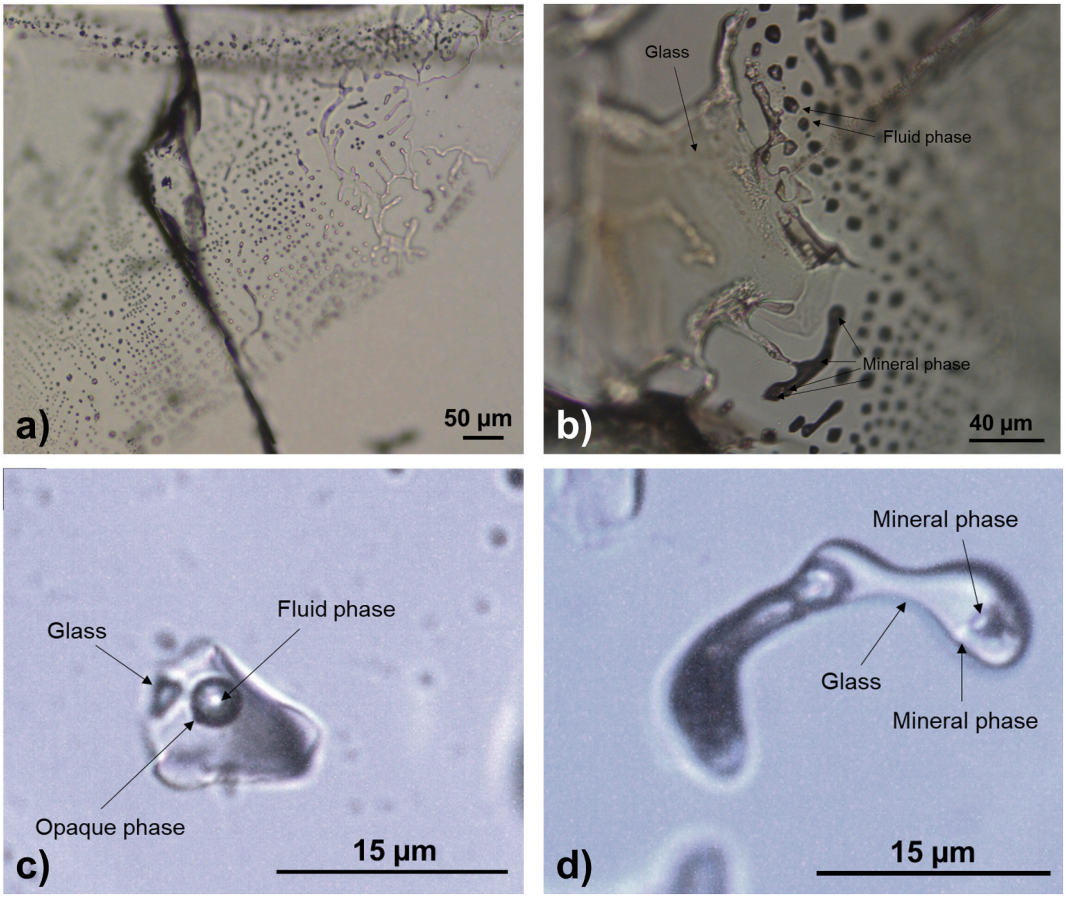

Fig. 2. Microphotograph of the inclusions in Hyblean olivine. (a) Multiple dendritic intergranular trails. (b) Dendritic trail originated from a glass microvein. Inclusions are made of fluid and birefringent mineral phases and, in some cases, show evidence of the negative crystal shape development. (c) Sub-rounded inclusion consists of glass, fluid, and an opaque mineral phase. (d) Elongated dendritic inclusions with glass texturally associated with birefringent mineral phases.

xenolithic nodules, the original names (i.e., HYB) adopted by Perinelli et al. (2008) are here replaced with VG (the acronym standing for Valle Guffari), maintaining the same numbers as in this previous manuscript. These eight xenoliths (VG14, VG21, VG23, VG24, VG29, VG34, VG36 and VG40) were described as subrounded in shape, ranging from ~5 cm to ~9 cm in size and classified as spinel lherzolites and spinel harzburgites according to the mineral modal abundance summarized in Table 1 and shown in Fig. 1. The main features (e.g., grain size, mineral habit, etc.) of the investigated samples are reported in detail in the Supplementary Materials, where we also emphasize the degree of preservation for the minerals primarily investigated for the aim of this study, such as olivine (ol) and spinel (spl), along with their textural

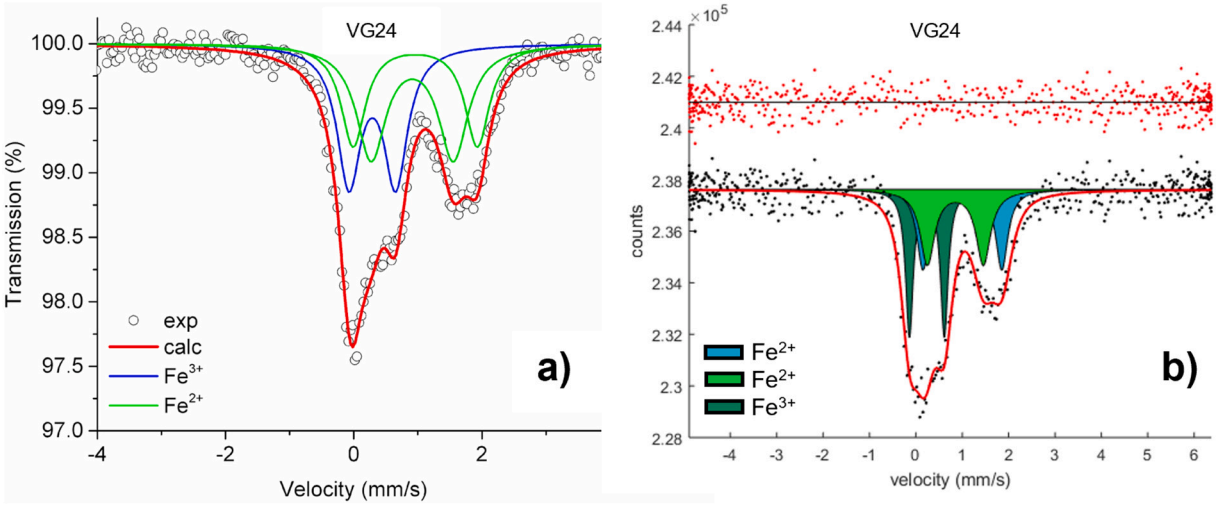

Fig. 3. The ^{57}Fe Mössbauer spectra of spinels from lherzolite VG24 collected with both a) conventional Mössbauer and (b) in-situ SMS, fitted with three-doublet model using a Lorentzian curve. The same $Fe^{3+}/\sum Fe$ ratio (0.35) was obtained using the two techniques.

features.

The chemical compositions of the bulk rock and each rock-forming mineral are those reported by Perinelli et al. (2008) and in Table S1a-d of the Supplementary Materials. Here we underline the Mg number (Mg#) of olivine, calculated as Mg/(Mg + Fe) mole ratio, of the investigated lherzolitic samples ranging from 0.89 (sample VG40) to 0.91 (sample VG14), while harzburgitic samples show Mg# of 0.91 for both VG29 and VG36. Orthopyroxenes (opx) are solid solutions of enstatite (88–91%), ferrosilite (8–9%) and wollastonite (1–2%), with Mg# comparable between lherzolites (0.90–0.91) and harzburgites (from 0.91 in VG29 to 0.92 in VG36). Clinopyroxenes (cpx) are diopsides with wollastonite (45–49%), enstatite (48–50%) and ferrosilite (4–6%) end members composition. Spinels from these peridotite rocks are generally solid solutions of noble spinel (55%), hercynite (20%), and Mg-chromite (25%) end members. Their Cr# (Cr/(Cr + Al) mole ratio) in lherzolites varies between 0.26 (VG14 and VG40) and 0.34 (VG23 and VG34); while the Cr# in harzburgites shows values of 0.29 (VG36) and 0.36 (VG29). Clinopyroxenes are enriched in light rare earth elements (LREE), particularly La, showing a positive correlation with Nb, V, Sr, U and Th, which were related to an oxidizing metasomatic event (Perinelli et al., 2008). Olivine, orthopyroxene and clinopyroxene in both lherzolites and harzburgites have homogeneous compositions from core to rim. In contrast, spinels from lherzolite VG24 and harzburgite VG29 register high variation in Al_2O_3 and Cr_2O_3 (i.e., the Cr#) from core to rim (Table S1d of the Supplementary Materials).

2.2. Petrographic description of fluid and melt inclusions

The presence of inclusions in the selected samples was preliminarily noted on the available petrographic thin sections (Fig. S1a-f of the Supplementary Materials). Olivine, clinopyroxene, and orthopyroxene all contain abundant trails of dendritic (vermicular) inclusions (Fig. 2a and b) in both lherzolitic and harzburgitic samples. A more accurate optical analysis was performed on selected thin sections double-polished to 150–180-μm thickness using a Leica DM750P polarized optical microscope at 40 X magnification. The petrographic study showed that these inclusions consist of glass, (daughter) minerals, and often a vapor phase. The morphology of these inclusions resembles that described by Sapienza et al. (2005); see their Fig. 3) also in the case of Hyblean mantle xenoliths from the Valle Guffari, although there are no geographic indications that their rock samples correspond to those investigated in this study. Trails of dendritic inclusions originate from the glassy microveins permeating the crystals over 200 to 500 μm of distance (Fig. 2b). The association of inclusions displayed in Fig. 2 occurs within the same olivine crystal from samples VG14 (lherzolite; Fig. 2c) and VG36 (harzburgite; Fig. 2d), respectively. The samples VG14 and VG36 exhibit inclusions with similar features, all with a secondary origin ranging from 5 to 40 μm in diameter and habits reflecting different degrees of maturity. Inclusions with the elongated dendritic habit (diameter from 20 to 40 μm) show the presence of glass texturally associated with mineral phases (Fig. 2d), while smaller inclusions (<15 μm) with subrounded shape are dominated by glass and/or a fluid phase (Fig. 2c). Features like necking-down from dendritic inclusion are frequent in both samples (Fig. 2a and b), while only a few inclusions in sample VG14 show a developed negative crystal shape (Fig. 2b). The observed silicate glass (Fig. 2b-d) is from colorless to brownish and isotropic under the crossed polarizers (Nicol X); while tiny crystals (<5 μm) show high relief and are sub-euhedral with both high birefringence (Fig. 2b and d) and opaque (Fig. 2c). The fluid is CO_2-rich (see paragraph 3.4) coexisting texturally with one or two phases (glass and glass + crystal).

Trails of dendritic inclusions in clinopyroxene and orthopyroxene are less abundant in both VG14 and VG36 and do not follow any preferential direction (e.g., exsolution lamellae or cleavage planes) as reported by Sapienza et al. (2005; Figure S2a and 2b of the Supplementary Materials).

Table 2
Hyperfine parameters (CS and QS), Area% and $Fe^{3+}/\sum Fe$ ratio for the analyzed spinels.

Sample	CS (mm/s)	QS (mm/s)	Area %	Assignment	$Fe^{3+}/\sum Fe$ ratio
VG14	0.29	0.75	32	Fe^{3+}	
	0.94	1.91	31	Fe^{2+}	0.32 (2)
	0.91	1.20	37	Fe^{2+}	
VG21	*0.28*	*0.78*	*33*	*Fe^{3+}*	
	0.97	*1.85*	*30*	*Fe^{2+}*	*0.33 (2)*
	0.91	*1.16*	*37*	*Fe^{2+}*	
VG23	*0.28*	*0.74*	*31*	*Fe^{3+}*	
	1.02	*1.75*	*31*	*Fe^{2+}*	*0.31 (2)*
	0.90	*1.19*	*38*	*Fe^{2+}*	
VG24	0.29	0.73	35	Fe^{3+}	
	0.96	1.94	28	Fe^{2+}	0.35 (3)
	0.91	1.28	37	Fe^{2+}	
VG24	*0.24*	*0.75*	*35*	*Fe^{3+}*	
	1.01	*1.70*	*31*	*Fe^{2+}*	*0.35 (3)*
	0.85	*1.21*	*34*	*Fe^{2+}*	
VG29	0.32	0.61	32	Fe^{3+}	
	0.90	2.02	27	Fe^{2+}	0.32 (2)
	0.90	1.25	41	Fe^{2+}	
VG34	0.29	0.74	34	Fe^{3+}	
	1.00	1.92	13	Fe^{2+}	0.34 (3)
	0.94	1.35	53	Fe^{2+}	
VG36	*0.29*	*0.77*	*31*	*Fe^{3+}*	
	1.05	*1.85*	*23*	*Fe^{2+}*	*0.31 (2)*
	0.93	*1.21*	*46*	*Fe^{2+}*	
VG40	*0.26*	*0.79*	*30*	*Fe^{3+}*	
	0.96	*1.82*	*34*	*Fe^{2+}*	*0.30 (2)*
	0.90	*1.10*	*36*	*Fe^{2+}*	

Notes: measurements performed by SMS are reported in italics.
Estimated standard errors: CS ± 0.02 mm/s; QS ± 0.05 mm/s.

2.3. Analytical techniques

In order to retrieve enough crystalline material with minimal contamination caused by the host lava and/or alteration (e.g., excessive serpentinization), each peridotite nodule was first deprived of its most superficial part by removing the exposed surface with a diamond blade and, then, crushed to proceed with a hand-picked selection of fresh spinel and olivine grains under the stereo microscope.

2.3.1. Scanning electron microscopy (SEM) and electron probe microanalyzer (EPMA)

A few hand-picked spinel and olivine crystals were mounted on a stub and analyzed using a FEI Quanta 400 scanning electron microscope with EDAX Genesis analyzer (voltage of 15 and 20 keV and current of 15 nA) available at the Department of Earth Sciences (Sapienza University of Rome, Italy). Analyses were performed to verify the extent of alteration and/or serpentinization and detect the possible presence of additional exsolved phases in both spinel and olivine (see Fig. S3a-b of the Supplementary Materials). Three single spinel crystals selected for in situ Mössbauer analyses (see next session) from samples VG21, VG23, and VG36 were also analyzed by the Cameca SX50 electron probe microanalyzer at CNR-IGAG, c/o Department of Earth Sciences of Sapienza University of Rome, Italy. The analytical conditions were 15 kV accelerated voltage and 15 nA beam current with a focused beam spot. The employed standards consisted of wollastonite for Si and Ca, corundum for Al, periclase for Mg, magnetite for Fe, Cr_2O_3 for Cr, rutile for Ti, pure Mn for Mn and jadeite for Na. The results of these analyses are reported in Table S2 of the Supplementary Materials.

2.3.2. Conventional and in situ synchrotron Mössbauer spectroscopy

The $Fe^{3+}/\sum Fe$ ratio of spinels was determined through Mössbauer spectroscopy. The hand-picked spinels from xenoliths VG14, VG24, VG29, and VG34 were ground under ethanol with an agate mortar, and the recovered fine powder (10–40 mg) was mixed with acrylic resin (Lucite) to make a disc of 10 mm of diameter and 1 mm thick,

Table 3
Pressure and temperature of equilibrium (from Perinelli et al., 2008 and Taylor, 1998) and logfO_2 (ΔFMQ) calculated using different spinel compositions, core, rim and single crystal (samples VG21, VG23, VG36). In *italics* logfO_2 calculated using $Fe^{3+}/\Sigma Fe$ measured through in situ SMS.

Sample	P (GPa)	T* (°C)	T ** (°C)	logfO_2 (ΔFMQ) (spl core)	logfO_2 (ΔFMQ)$^+$ (spl core)	logfO_2 (ΔFMQ) (spl rim)	logfO_2 (ΔFMQ) (spl single crystal)
VG14	1.20	1007	1259	0.32	0.24	0.47	–
VG21	1.23	1053	1252	*0.28*	*0.22*	*0.39*	*0.21*
VG23	1.13	1001	1208	*0.45*	*0.40*	*0.49*	*0.21*
VG24	1.13	1036	1237	0.66	0.60	0.67	–
VG29	1.12	1034	1310	0.75	0.70	0.68	–
VG34	0.95	957	1106	1.15	1.10	–	–
VG36	1.30	911	1073	*1.27*	*1.22*	*1.16*	*1.05*
VG40	0.85	873	1054	*1.18*	*1.08*	*1.06*	–

Notes: (*) T as reported by Perinelli et al. (2008); (**) T calculated using Taylor (1998); ($^+$) logfO_2 calculated with T from Taylor (1998).

corresponding to an absorber density below 5 mg Fe/cm^3. The absorber was, then, loaded in a Plexiglas sample holder with a diameter of 1 cm. Measurements were performed using a spectrometer with a conventional ^{57}Co source of 0.99 GBq (25 mCi) embedded in a 7 mm Rh matrix at the Earth Sciences Department of Sapienza University of Rome. The spectra were collected in 2–3 days in transmission mode within the velocity range of −4 - +4 mm/s and recorded with a multichannel analyzer. The velocity was calibrated using a 25-μm thick α-iron foil. The obtained spectra were fitted to a Lorentzian line shape using the RECOIL 1.04 fitting program.

For those samples with low modal abundance (VG36) or with few suitable single crystals after crushing the rock sample (VG21, VG23 and VG40), the $Fe^{3+}/\sum Fe$ ratio of spinels was measured using in situ synchrotron Mössbauer spectroscopy (SMS) at the ID18 nuclear resonance beamline of the European Synchrotron Radiation Facility (ESRF, Grenoble, France). Here, the Mössbauer characteristic energy is obtained using the 111 Bragg reflection of $^{57}FeBO_3$ single crystal mounted on a Wissel velocity transducer driven with a sinusoidal waveform at room temperature (Potapkin et al., 2012). The X-ray beam was focused onto an area of 15 × 10 μm^2 using Kirkpatrick-Baez mirrors. The velocity scale was calibrated using a 25-μm thick α-Fe foil. Spectra were also fitted using a full transmission integral with normalized Lorentzian-squared source lines through the MossA software package (Prescher et al., 2012). About 1–2 h were required to collect each spectrum. The SMS measurements were corrected to account for the signal (~1%) caused by the presence of Fe contamination in the Be window (Marras et al., 2023).

The $Fe^{3+}/\sum Fe$ ratio of spinels from VG24 was analyzed with conventional and SMS techniques to test the reproducibility of the results between bulk and punctual analyses (see Table 2 and Fig. 3a and b). All the spectra were fitted with two doublets for Fe^{2+} and one for Fe^{3+} (Fig. 3a and b and Fig. S4a-f of the Supplementary Materials) according to the model proposed by Canil and O' Neill (1996) (Table 2 and Fig. S5 of the Supplementary Materials). If the correction proposed by De Grave and Van Alboom (1991) for the effect of temperature is applied to our data, the determined $Fe^{3+}/\sum Fe$ ratios decrease by ca. 0.05 with respect to those listed in Table 2.

2.3.3. Noble gases measurements

Noble gases analyses were performed on 1.00–1.59 g of accurately selected olivine single crystals from each grinded peridotite sample. Samples VG21 and VG40 were excluded from the analysis due to low material availability (<0.80 g). Noble gases isotopic analyses were carried out at the Istituto Nazionale di Geofisica e Vulcanologia (INGV-Palermo) following the preparation and analytical protocols described by Rizzo et al. (2018). Hand-picked olivine grains were cleaned in acetone and millipore water by using an ultrasonic bath, and the portion of the selected sample material was loaded into a stainless-steel crusher baked for 48–72 h at 120 °C in order to achieve ultra-high-vacuum conditions (10^{-9} mbar). Fluid inclusions from minerals were released by an in-vacuum single-step crushing, and the external pressure applied to the minerals by the hydraulic press was 250 bar. Noble gases were separated from the other volatiles by using a "cold finger" immersed in liquid nitrogen ($T = -196$ °C) that allows freezing H_2O and CO_2, and successively were further cleaned in an ultra-high vacuum (10^{-9}–10^{-10} mbar) purification line, and all the species of the gas mixture, except noble gases, were removed using four getters. Helium (^{3}He and ^{4}He) and neon (^{20}Ne) isotopes were measured separately by two different split-flight-tube mass spectrometers (Helix SFT-Thermo). The analytical uncertainty of He isotopic ratio is ≤4%. The ^{20}Ne isotope ratio was corrected for isobaric interferences at m/z values of 20 ($^{40}Ar^{2+}$). Argon isotopes (^{36}Ar, ^{38}Ar and ^{40}Ar) were analyzed by a multi-collector mass spectrometer (GVI Argus) with an analytical uncertainty of 1.0%. The uncertainty in the determinations of He, Ne, and Ar elemental contents is <5%.

2.3.4. Micro-Raman and micro-transmittance Fourier transform infrared spectroscopy

Double-polished thin sections (180-μm thick) of samples VG14 (lherzolite) and VG36 (harzburgite) were prepared for micro-Raman and micro(μ)-transmittance(T) FTIR analysis mostly on olivine crystals. Raman analyses were performed to investigate the fluid composition and identify possible mineral and/or melt inclusions. A Labram HR Evolution (Horiba Scientific, Japan) Raman spectrometer was employed at the Department of Earth and Environmental Sciences of Milano-Bicocca University. Spectra were recorded by a green 532 nm laser source (300 mW) using a 25% neutral density filter through a transmitted light Olympus B40 microscope with a 100× objective. The analytical setup consisted of a confocal pinhole of 100 μm and a 600 g/mm diffraction grating, allowing a spatial resolution of 1 μm^3. Acquisition time was 30 s for measurement. A silicon standard (520 cm^{-1}) was used for linear spectrometer calibration with a precision of ±1 cm^{-1}. A total of 30 spectra were acquired from olivines of both sample VG14 and VG36, plus 15 additional spectra also collected on opx and cpx for comparative analyses.

The FTIR measurements were performed at the SISSI beamline of ELETTRA synchrotron (Trieste, Italy) to verify the presence of H_2O in the inclusions of the same olivine grains analyzed by Raman. The data were collected using a Vertex 70 V Bruker interferometer coupled with a conventional Globar infrared source, a Hyperion IR microscope and a mercury cadmium telluride (MCT) detector to focus and resolve the areas of interest in the full spectral range. The spectra were collected in transmission mode with a resolution of 2 cm^{-1} and an aperture of 40 μm. A total of 65 spectra from VG14 and 30 from VG36 were acquired on regular grids with areas of ~400 × 300 μm^2 and ~ 250 × 200 μm^2, respectively, with steps of 40 μm in both directions (X and Y; see Figs. S6a and 6b and S7a and 7b of the Supplementary Materials). The signal was averaged for 256 scans (256 s) on each measurement spot. The spectrum of air was collected as a reference before and after the measurements.

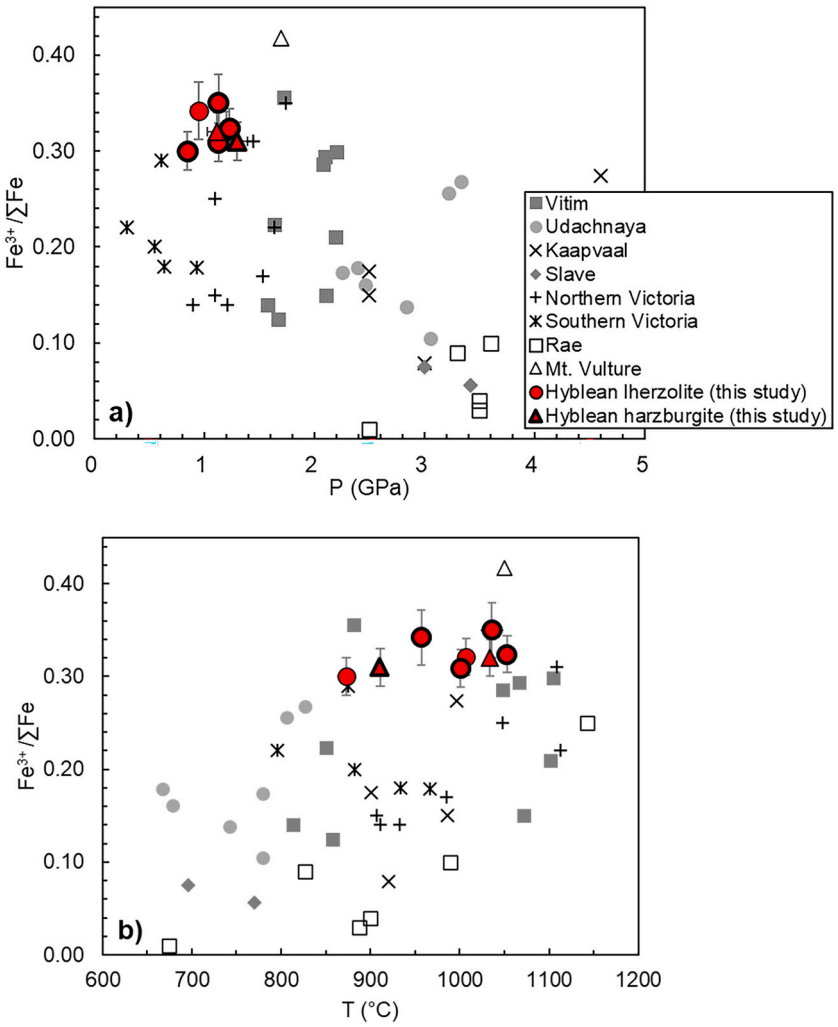

Fig. 4. $Fe^{3+}/\sum Fe$ vs (a) pressure (GPa), (b) temperature (°C) for lherzolitic and harzburgitic Hyblean spinels compared with those from spinel-peridotites from literature (see references in the text). Symbols with thick edges refer to spinels measured by in-situ SMS. The error bars of P and T for the Hyblaean samples (this study) are within the symbols size.

3. Results

3.1. Pressure and temperature of equilibration

Our reported P-T conditions of equilibration (Table 3) for the selected xenoliths are from Perinelli et al. (2008) calculated according to the olivine-clinopyroxene Ca exchange geobarometer (Köhler and Brey, 1990) and the two-pyroxene geothermometer (Brey and Köhler, 1990), respectively. Although the Brey and Köhler (1990) two-pyroxene thermometer tends to overestimate T, especially for Na-rich peridotitic cpx (Nimis and Grütter, 2010), the low Na content of cpx from this study ranging between 0.02 and 0.10 atoms per formula unit (apfu), results in an overestimation of +30 °C, i.e. within the error of the Brey and Köhler (1990) calibration. The calculated P varies from 0.85 GPa (±0.04; VG40) to 1.23 GPa (±0.01; VG21) with T between 873 °C (VG40) and 1053 °C (VG21) in the case of lherzolitic samples, and from 1.12 GPa (±0.07; VG29) to 1.30 GPa (±0.05; VG36) with T between 911 °C (VG36) and 1034 °C (VG29) in the case of harzburgitic samples. These estimates indicate the variability introduced by olivine compositional changes within the same sample for which the additional uncertainty of the Ca-in-Ol barometer calibration (i.e., 0.17 GPa), and the strong T-dependence of the barometer (~ 0.4 GPa/30 °C) must be considered. For comparison, we also employed Taylor (1998) geothermometer, from which a higher T varying from ~150 °C (VG34) to 275 °C (sample VG29) is obtained (Table 3). In contrast, due to the limited exchange reactions available as well as the lack of experiments representative of multi-component systems, P of spinel peridotites remains poorly constrained (MacGregor, 2015). It was suggested by O'Neill (1981) and successively by Klemme (2004) that a high concentration of Cr in spinel (Cr# > 0.20) could be indicative of greater depths (i.e., high P) as a result of the effect of Cr on the spinel stability field. According to thermodynamic modelling (Ziberna et al., 2013), peridotitic spinel and garnet are stable over different depth intervals, depending on the thermal regime and peridotite fertility. On a hot geotherm such as that estimated for the Hyblean peridotites (Nimis, 1998), the spinel field would extend to about 50 km depth, while spinel and garnet would coexist at about 50–70 km depths. Therefore, the maximum P for the Hyblean spinel peridotites is 1.5 GPa, implying greater maximum depths than originally suggested by Scribano and Carbone (2020) for serpentinized spinel peridotites. Noteworthy, the effect of different processes on spinel Cr# (i.e., the spinel/garnet transition), such as melt extraction (e.g., Hellebrand et al., 2001), melt addition (Birner et al., 2021) and metasomatism (El Dien et al., 2019) should be also considered.

3.2. The Fe oxidation state of spinels

The measured $Fe^{3+}/\sum Fe$ ratios of spinels are summarized in Table 2, along with the center shift (CS) and quadrupole splitting (QS) hyperfine

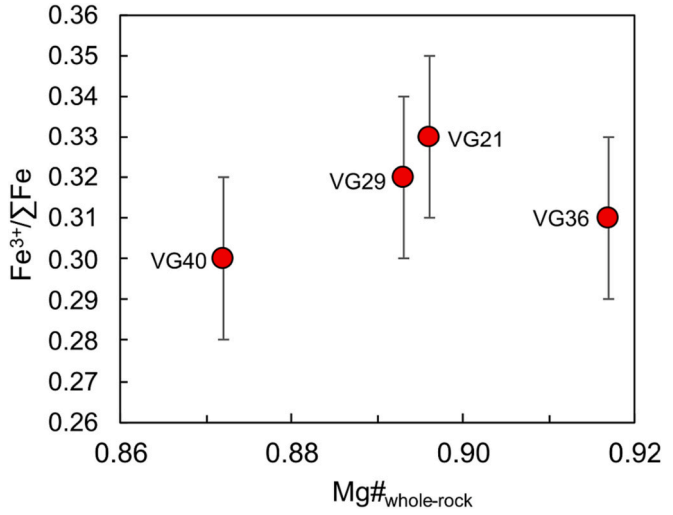

Fig. 5. Plot of $Fe^{3+}/\sum Fe$ ratio of spinel (this study) vs Mg# of whole-rock (Perinelli et al., 2008) for samples VG21, VG29, VG36 and VG40. Error bars for $Fe^{3+}/\sum Fe$ are reported.

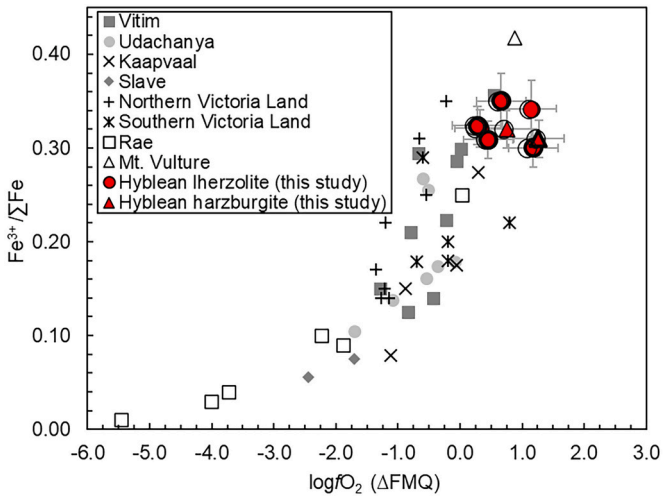

Fig. 6. $Fe^{3+}/\sum Fe$ vs logfO_2 (ΔFMQ) for Hyblean peridotites from this study plotted along with literature data (see the references in the text). Symbols with thick edges refer to samples measured by in-situ SMS. LogfO_2 of the Hyblean samples calculated with T from Taylor (1998; T98) thermometer is reported for comparison (empty symbols).

values. The hyperfine parameters are shown in Fig. S5 of the Supplementary Materials and compared with reference data from Canil and O' Neill (1996). The $Fe^{3+}/\sum Fe$ ratio of spinels analyzed by conventional Mössbauer (bulk analysis; VG14, VG24, VG29 and VG34) ranges between 0.32 and 0.35; while that by in-situ SMS (punctual analysis; VG21, VG23, VG36 and VG40) ranges between 0.30 and 0.35. The $Fe^{3+}/\sum Fe$ ratio of sample VG24 was 0.35 by both techniques, providing evidence of data reproducibility and homogeneity. The $Fe^{3+}/\sum Fe$ ratio of lherzolitic spinels overlaps with that of harzburgitic spinels, ranging from 0.30 to 0.35 and 0.31 to 0.32, respectively. Fig. 4a and b show the measured $Fe^{3+}/\sum Fe$ ratios plotted as a function of the estimated equilibration P and T (Perinelli et al., 2008) compared with data for spinels also measured by Mössbauer from peridotites of various cratonic areas worldwide like Northern and Southern Victoria Land Antarctica (Martin et al., 2015; Perinelli et al., 2012, 2014), Kaapvaal (Woodland and Koch, 2003), Rae (Woodland et al., 2021), Slave (McCammon and Kopylova, 2004), Udachnaya (Goncharov et al., 2012), Vitim (Goncharov and Ionov, 2012) and Mt. Vulture (Marras et al., 2023). Compared to the literature peridotite data, spinels from this study are among those with the highest $Fe^{3+}/\sum Fe$ ratios. No correlation is observed among $Fe^{3+}/\sum Fe$ ratios and P and T for the Hyblean spinels in contrast with the positive trend reported for T in the case of Vitim and Rae (Goncharov and Ionov, 2012; Woodland et al., 2021). Moreover, the spinel Fe^{3+} apfu versus $Cr\#_{spinel}$ plot (Fig. S8 of the Supplementary Materials) shows no visible trend for the Hyblean samples as, instead, shown in the case of xenoliths and orogenic massif peridotites and explained as the result of the energetically favored Fe^{3+}-Cr cation substitution (Canil and O' Neill, 1996). Following the rationale by Canil and O' Neill (1996), the absence of a positive correlation, as shown by Ballhaus et al. (1991), may be the result of the combination of different effects such as (1) the increase of melt extraction with consequent increase of Cr# (decreasing of the incompatible Fe^{3+}), and (2) the increase of Fe^{2+} that correlates with Cr#. In addition, some correlation between bulk Mg# and the spinel $Fe^{3+}/\sum Fe$ should appear as result of the incompatible behavior of Fe^{3+} during melt extraction. However, both Fig. S8 and Fig. 5 do not reveal the expected trends. This is likely due to the possibility that Hyblean spinel crystal chemistry (i.e., Mg, Fe^{2+}, Fe^{3+}, Al^{3+} and Cr apfu, Cr# and Mg#) and its oxidation state (expressed by the $Fe^{3+}/\sum Fe$ ratio) have been masked by chemical interactions with (oxidized) fluids (Arai, 1994).

3.3. *Oxy-thermobarometry of the selected Hyblean mantle peridotites*

The fO_2 of the selected spinel-peridotite xenoliths was determined using the oxy-thermobarometer calibrated by Ballhaus et al. (1991) from the measured $Fe^{3+}/\sum Fe$ of spinel (this study) at the equilibration P-T values (Perinelli et al., 2008) obtained by a combination of the Brey and Köhler (1990) two-pyroxene thermometer and Köhler and Brey (1990) Ca-in-olivine barometer, employing the chemical compositions of coexisting olivine, opx and spinel (core composition). For comparison, we also show the fO_2 calculated using the T obtained from Taylor (1998) model. The calculated fO_2s were normalized to the fayalite-magnetite-quartz buffer (FMQ; see Table 2 of Ballhaus et al., 1991) and are summarized in Table 3. The logfO_2 varies from 0.28 to 1.18 log units (ΔFMQ) in the case of lherzolites, and from 0.75 to 1.27 in the case of VG29 and VG36 harzburgites. A general maximum uncertainty of ±0.4 log units propagates when P, T, $Fe^{3+}/\sum Fe$, thermodynamic and EPMA data are combined (Ballhaus et al., 1991). More in detail, a variation of T by 50 °C would cause the fO_2 to shift by ±0.03 log units; while a variation of P by 0.5 GPa would cause the fO_2 to vary by ±0.15 log units. It can be noted that logfO_2 values calculated based on the measured $Fe^{3+}/\sum Fe$ contents are equal to or slightly higher (up to 0.2 log units, i.e., within the uncertainty of the oxy-thermobarometer) than the fO_2 values calculated when the Fe^{3+} data are corrected for the temperature effect. The lherzolitic sample VG21 is the most reduced sample (0.28 log units), while the harzburgitic VG36 is the most oxidized with logfO_2 of 1.27 (ΔFMQ). Using spinel rim compositions instead of core compositions, the logfO_2 (ΔFMQ) decreases only by 0.2 log units in samples VG29, VG36 and VG40 and increases by 0.15 log units in samples VG14 and VG21; while in the case of VG23 and VG24, the calculated fO_2 is unchanged (see Table 3). In the case of samples VG21, VG23 and VG36, we determined the logfO_2 according to the composition measured on the spinel single crystals (Table S2 of the Supplementary Materials), and it decreased by 0.2 log units in all the samples (Table 3). Fig. 6 shows a linear correlation between logfO_2 (ΔFMQ) and $Fe^{3+}/\sum Fe$ ratio of spinels from the global database, including the Hyblean spinel peridotites. Fig. 7a and b show that the negative effect of P and T on the logfO_2 (ΔFMQ) of the Hyblean samples is maintained even when the propagated P and T uncertainties (see above) are considered, in agreement with what was proposed by Ballhaus et al. (1991). Notably, the fO_2 calculated using the T estimates from Taylor (1998) does not change significantly, and both Figs. 6 and 7a-b

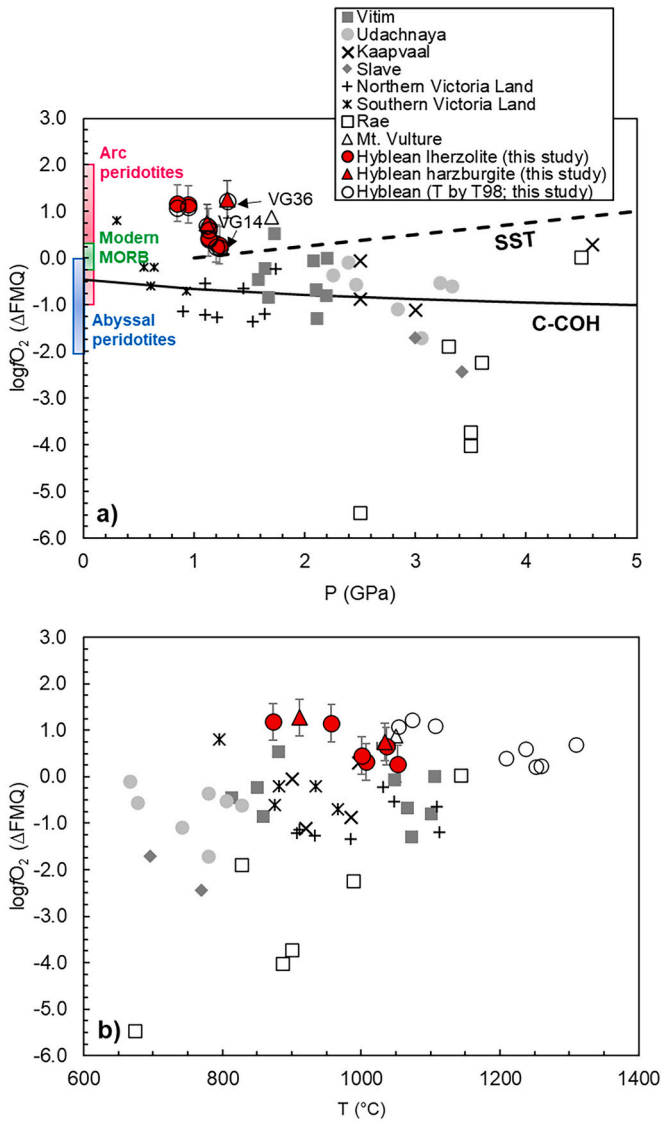

Fig. 7. LogfO$_2$ (ΔFMQ) plotted as a function of (a) P and (b) T with literature data (see references in the text), along with the logfO$_2$ of Hyblean peridotites calculated using Taylor (1998; T98) geothermometer. (a) Reference values for MORB (Cottrell et al., 2021), abyssal (Birner et al., 2018; Bryndzia and Wood, 1990) and arc peridotites (Cottrell et al., 2021) are shown. The reference buffer C-COH (Ulmer and Luth, 1991) is reported along with the sulfide-to-sulfate transition line (SST) from Chowdhury and Dasgupta (2020). Samples VG14 and VG36 are indicated by arrows. The error bars of P and T for the Hyblaean samples (this study) are within the symbols size.

confirm that the fO_2 determined for the Hyblean peridotites are the highest among those from the literature dataset.

3.4. Spectroscopic characterization of the fluid inclusions in olivine

We collected Raman spectra on the inclusions in olivine crystals from two samples VG14 lherzolite and VG36 harzburgite, which are the most reduced (0.32 log units ΔFMQ) and the most oxidized (1.27 log units ΔFMQ), respectively. Preliminary optical analyses of these samples in thin sections also revealed the presence of many tiny inclusions, which made the selected samples suitable to be analyzed. The most representative spectra are shown in Figs. 8a-c and Fig. S9a of the Supplementary Materials for the reduced VG14 sample, and Figs. 8d-f and Fig. S9b of the Supplementary Materials for the oxidized sample VG36, and show differences in the composition of the inclusions. For instance, the dominant fluid phase in olivine of VG14 is CO_2 (Fig. 8a and c), identified by the Fermi doublet at about 1281 cm^{-1} and 1386 cm^{-1}. Brownish microveins of (silicate) glass in olivine crystals were identified by broad peaks in the Raman spectra. The (daughter) mineral texturally associated with the silicate glass is Mg-calcite with typical vibrations at 282 cm^{-1}, 714 cm^{-1} and 1087 cm^{-1} (Fig. 8b). Pure magnesite was also identified by the main vibrations at 210, 740, and 1093 cm^{-1} (Fig. S9a of the Supplementary Materials). The Raman peaks of carbonates are weak and broad (full width at half maximum, FWHM, up to 16 cm^{-1}) when compared to those reported, for instance, by Sandoval-Velasquez et al. (2021a), likely linked to the disorder and/or low crystallinity (Frezzotti et al., 2012a) as it occurs in the case of structurally unstable crystalline carbonates or fast crystallization from fluids (Frezzotti et al., 2012a; Frezzotti and Peccerillo, 2007). Tiny opaque mineral grains are observed, the peaks of which have wave numbers corresponding to both native S with strong vibrations at 150 cm^{-1}, 218 cm^{-1}, and 468 cm^{-1} and a sulfide mineral, pyrite, with vibrations at 324 cm^{-1} and 375 cm $^{-1}$ (Fig. 8c). Interestingly, 3 out of 12 analyzed inclusions in VG14 contained only CO_2 fluids (see Fig. 8a). Inclusions with only CO_2 as the trapped phase are even less frequent (1 of the 15 analyzed) in sample VG36 (the most oxidized). Here, inclusions also consist of glass and (daughter) minerals in mutual contact. Figs. 8d-e show two representative Raman spectra characterized by coexisting sulfates with different compositions, such as the Na-Ca end member, glauberite (identified bands at 648 cm^{-1}, 1000 cm^{-1} and 1138 cm^{-1}), the Na-pure thenardite and Na-pure carbonated burkeite with overlapped main vibrations at 450 cm^{-1}, 620–630 cm^{-1} and 994–996 cm^{-1}, while characteristic peaks are those at 474 cm^{-1} for burkeite and 469 cm^{-1} and 1153 cm^{-1} for thenardite (Figs. 8d-e). Barite is also observed, with peaks at 459 cm^{-1}, 617 cm^{-1} and 987 cm^{-1} (Fig. 8e). Carbonates also occur like dolomite (175 cm^{-1}, 299 cm^{-1} and 1098 cm^{-1}), magnesite (210 cm^{-1}, 327 cm^{-1} and 1094 cm^{-1}) and Mg-calcite (154 cm^{-1}, 714 cm^{-1} and 1087 cm^{-1}1; Figs. 8e-f and Fig. S9b of the Supplementary Materials). Sulfates and carbonates vibrations are downshifted by 2 to 4 cm^{-1} from reference positions (Frezzotti et al., 2012a), likely due to minor mineral formula variations. Few spectra were also collected on opx and cpx of VG14 and VG36 (Figs. S9c-d of the Supplementary Materials). These inclusions appear dominated by dolomite and CO_2 in cpx from both samples, while inclusions in opx are similar to those described in olivine with sulfides and sulfates (+ carbonate) in sample VG14 and sulfates (+ carbonate) in VG36.

The presence of water in the fluid inclusions of both VG14 and VG36 olivines was investigated through the acquired FTIR maps (Figs. S6a and 6b and S7a and 7b of the Supplementary Materials). Selected grids of measurements were manually performed and include trails of inclusions in the same olivine single crystals analyzed by Raman spectroscopy. In sample VG14, strong absorption bands in the 3600–3800 cm^{-1} region correspond to the OH^- groups of minerals like talc or serpentine (Fig. S6a-b of the Supplementary Materials; Frezzotti et al., 2012a, 2012b) were observed in the portion occupied by the inclusions. No evidence of absorption in the molecular H_2O region (bands between 3000 and 3500 cm^{-1}) and OH^- region that could be assigned to daughter minerals was found in the surrounding olivine. In contrast, along fluid inclusion trails in olivine from sample VG36, we observed a strong absorption between 3000 and 3500 cm^{-1} (Fig. S7a-b of the Supplementary Materials). We conclude that VG14 and VG36 samples record interaction with an H_2O-bearing fluid. However, while the presence of OH^- groups in VG14 is associated with epigenetic hydration reactions (i.e., serpentinization) between fluid inclusions and the surrounding olivine wall, inclusions in VG36 retain a certain amount of molecular H_2O. The absence of OH^- bonds in the anhydrous surrounding olivine may indicate a fast diffusion of H^+ from the fluid inclusions. Sapienza et al. (2005) described pure CO_2 fluid inclusions with rare additional magnesite and anhydrite for the same suite of Hyblean peridotites. Although we cannot claim the same nature as the xenoliths studied here, we point out that the inclusions we observed are more chemically complex as they involve the coexistence of (Na-rich) S-

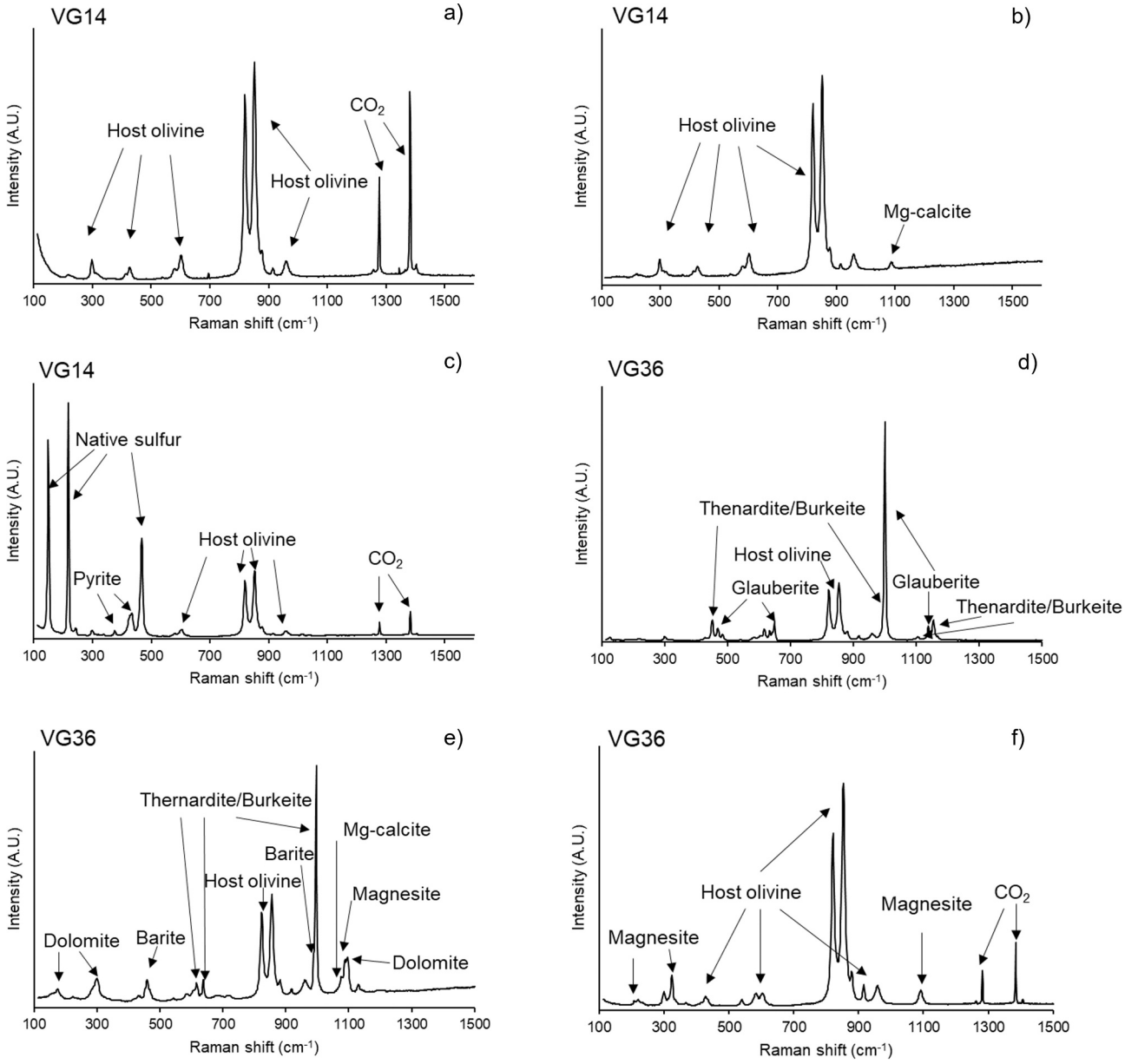

Fig. 8. Raman spectra of inclusions in olivines from lherzolite VG14 and harzburgite VG36. (a) Pure CO_2 fluid inclusion; (b) magnesite showing a weak and broad peak; (c) opaque phases, native sulfur and sulfide, shown in Fig. 2c; (d, e) Na-rich sulfates and barite, associated with glass as shown in Fig. 2d; (f) CO_2 associated with magnesite.

Table 4
Noble gases analysis on olivine crystals from Valle Guffari spinel-peridotites and weight of the analyzed samples.

Sample	Weight (g)	^{4}He (mol/g)	^{20}Ne (mol/g)	^{40}Ar (mol/g)	^{40}Ar* (mol/g)	^{4}He/^{40}Ar*	R/Ra	Err tot (+/−)	^{40}Ar/^{36}Ar	Err (%)	^{4}He/^{20}Ne
VG 14	1.49	3.39E-13	1.48E-16	3.96E-13	1.95E-13	1.74	7.12	0.10	589.70	0.19	2.29E+03
VG 23	1.55	1.63E-13	2.30E-17	1.20E-13	2.23E-14	7.30	7.22	0.12	366.77	0.41	7.09E+03
VG24	1.55	2.93E-12	3.94E-16	2.53E-12	2.06E-12	1.42	7.21	0.08	1589.54	0.10	7.43E+03
VG 29	1.52	1.34E-12	1.83E-16	1.30E-12	1.05E-12	1.28	7.04	0.09	1544.97	1.32	7.35E+03
VG 34	1.59	8.66E-14	1.19E-17	1.64E-13	3.77E-14	2.30	7.24	0.14	387.62	0.32	7.29E+03
VG36	1.00	8.11E-13	4.08E-16	7.08E-13	3.39E-13	2.39	7.28	0.10	573.16	0.11	1.99E+03

bearing minerals with carbonates, CO_2 and (secondary) hydrous phases.

3.5. Noble gases signature from inclusions in olivine crystals

The absolute concentration and isotopic composition of the olivine-hosted fluid inclusions from the Hyblean lherzolitic (VG14, VG23, VG24 and VG34) and harzburgitic (VG29 and VG36) samples are reported in Table 4. The ^{4}He concentration varies from 8.66×10^{-14} to 2.93×10^{-12} mol/g in the case of lherzolitic olivines and from 8.11×10^{-13} to 1.34×10^{-12} for harzburgitic olivines (Fig. 9) overlapping the data from previous studies (e.g., Correale et al., 2012; Sapienza et al., 2005). The lowest values are measured in sample VG34 (lherzolite). The

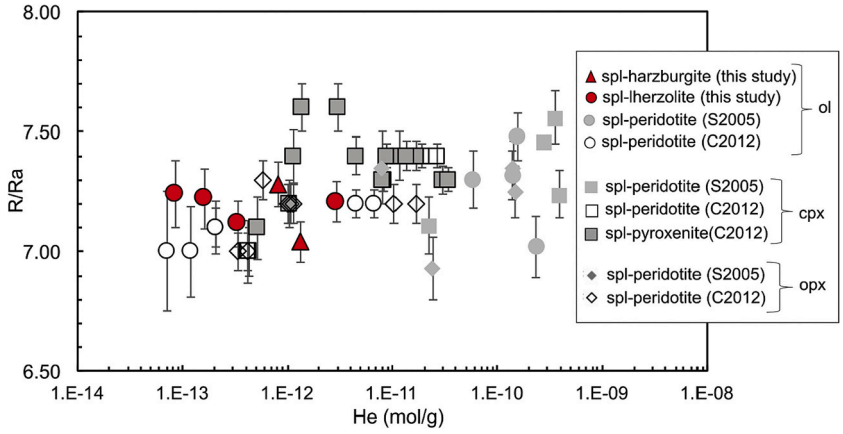

Fig. 9. R/Ra ratio vs He concentration (mol/g) measured from fluid inclusions of olivines (this study) compared with data for olivine, clinopyroxene and orthopyroxene extracted from Hyblean spinel-peridotites and pyroxenites from previous studies (Correale et al., 2012; Sapienza et al., 2005).

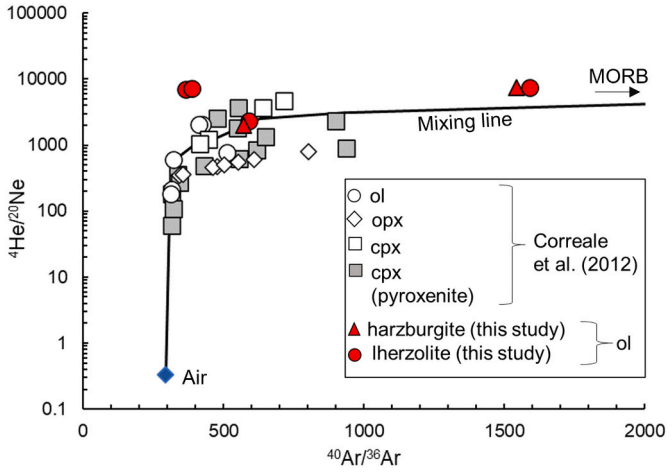

Fig. 10. $^4He/^{20}Ne$ vs $^{40}Ar/^{36}Ar$ ratios of Hyblean olivine (this study) compared with data from Correale et al. (2012) for Hyblean olivine, orthopyroxene and clinopyroxene both peridotitic and pyroxenitic. The mixing line was computed considering the end members MORB ($^4He/^{20}Ne \sim 10{,}000$ (Marty et al., 1983), $^{40}Ar/^{36}Ar \sim 40{,}000$ (Graham, 2002)) and air ($^4He/^{20}Ne = 0.318$, $^{40}Ar/^{36}Ar = 295.5$).

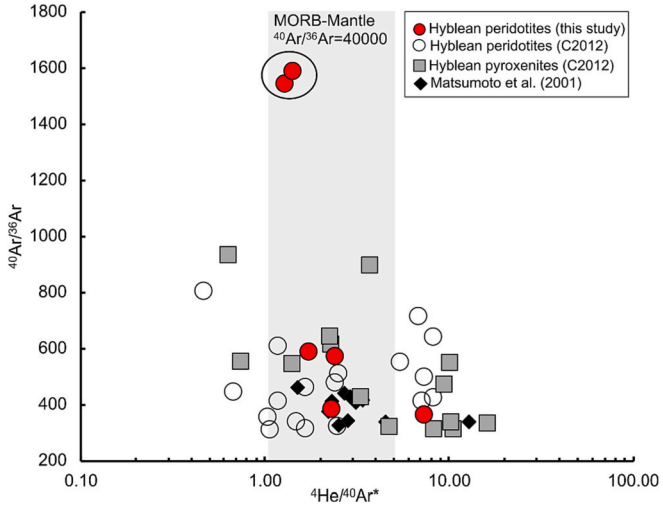

Fig. 11. $^{40}Ar/^{36}Ar$ ratios plotted versus the $^4He/^{40}Ar^*$ ratios for samples from this study along with Matsumoto et al. (2001) and Correale et al. (2012) data. Samples with the highest $^{40}Ar/^{36}Ar$ ratios (circled) that overlap the lowest values of the gases emitted in the peripheral region of Mt. Etna volcano (Mofeta dei Palici gas field; Correale et al., 2012 and references therein) have the $^4He/^{40}Ar^*$ ratios in the range of the mantle values (the data are discussed in Section 4.3).

concentration of ^{40}Ar varies between 3.96×10^{-13} and 2.53×10^{-12} mol/g in lherzolitic samples, and between 7.08×10^{-13} and 1.30×10^{-12} mol/g in harzburgitic samples. Finally, ^{20}Ne in both lherzolitic and harzburgitic olivines varies between 2.30×10^{-17} and 1.48×10^{-16} mol/g and between 4.08×10^{-16} and 1.83×10^{-16}, respectively. All these values overlap with data from Correale et al. (2012). For the VG14 (reduced) values are 3.39×10^{-13} for ^4He, 3.96×10^{-13} for ^{40}Ar, 1.48×10^{-16} for ^{20}Ne while for VG36 (oxidized) are 8.11×10^{-13} for ^4He, 7.08×10^{-13} for ^{40}Ar, 4.08×10^{-16} for ^{20}Ne. The $^4He/^{20}Ne$ and $^{40}Ar/^{36}Ar$ ratios are combined to evaluate the possible presence of an atmospheric component in the fluid inclusions (e.g., recycled through subduction or post-entrapment). Hyblean samples both from this study and Correale et al. (2012) fall along a mixing line between air (atmosphere) and a mantle end member MORB-type (Fig. 10). This confirms that measured gases were contaminated by the atmosphere, explained by Correale et al. (2012) mainly as an air component trapped in mineral cracks during or after the volcanic activity (Nuccio et al., 2008). However, the high $^{40}Ar/^{36}Ar$ ratios recorded in our fluid inclusions, up to 1544 (Figs. 10 and 11), are very close to the range of $^{40}Ar/^{36}Ar$ ratios (1600–2000) of the free gases at Mofete dei Palici (northern Hyblean area, 40 km from mt Etna volcano), which are consistent with mixing between a MORB mantle component and air (Correale et al., 2012 and references therein).

Furthermore, we also computed the amount of ^{40}Ar corrected for its atmospheric component ($^{40}Ar^*$; Graham, 2002), assuming an atmospheric origin for all the measured ^{36}Ar. The $^4He/^{40}Ar^*$ ratios vary between 1.28 and 7.30, which overlaps the typical production ratio of the mantle ($^4He/^{40}Ar^* = 1$–5; Yamamoto et al., 2009; Marty, 2012) except for the sample (VG23) that is characterized by the lowest $^{40}Ar/^{36}Ar$ (366.7; Fig. 11). These $^4He/^{40}Ar^*$ ratios overlap the previous data from the Hyblean products (Correale et al., 2012) that fall in a larger range (0.5–15.4) and indicate the occurrence of degassing processes and partial melting (Correale et al., 2012: see Fig. S10 of the Supplementary Materials).

4. Discussion

4.1. The redox state of the Hyblaean lithospheric mantle and geochemical evidence of the interaction with metasomatic fluids

Our estimates of $\log fO_2$ (ΔFMQ) calculated with the Ballhaus'

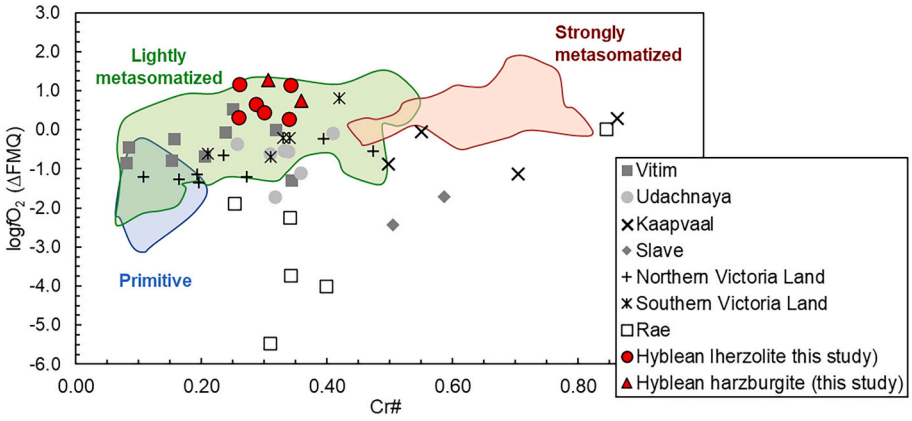

Fig. 12. LogfO_2 (ΔFMQ) vs Cr# for Hyblean peridotites and literature spinel-peridotites (see references in the text) plotted along three fields by Ballhaus et al. (1991) reflecting different degrees of metasomatism.

oxythermobarometry Ballhaus et al. (1991) for the investigated peridotite samples from this study (Table 3) are plotted in Fig. 7a and b along with spinel-peridotite xenoliths from Northern and Southern Victoria Land Antarctica (Martin et al., 2015; Perinelli et al., 2012, 2014), Kaapvaal (Woodland and Koch, 2003), Rae (Woodland et al., 2021), Slave (McCammon and Kopylova, 2004), Udachnaya (Goncharov et al., 2012), Vitim (Goncharov and Ionov, 2012) and Mt. Vulture (Marras et al., 2023). For consistency, the fO_2 of all the above-reported peridotite xenoliths were calculated using Ballhaus et al. (1991) oxythermobarometer, while the P and T are those recalculated by Miller et al. (2016) for which the proposed uncertainties of ±30 °C and ± 0.3 GPa are given that propagate to an fO_2 uncertainty of ±0.09 log units. On the other hand, the T correction adopted by employing other existing models like Jianping et al. (1995), for instance, has a negligible effect on the estimated fO_2 by <0.1 log units. A similar negligible effect is observed when a different geothermometer like that by Taylor (1998) is used (see Fig. 7a and b). The intervals representative of the fO_2 of MORB (logfO_2 ≃ FMQ; Cottrell et al., 2021) are also included along with the interval proposed for abyssal peridotites (−2 to 0 log units; Bryndzia and Wood, 1990; Birner et al., 2018; recalculated to use the Ballhaus et al. (1991) oxybarometer for consistency with the data reported here). Interestingly, Hyblean peridotites from Valle Guffari record higher logfO_2 than other spinel peridotites worldwide, even with respect to the present-day oceanic upper mantle (e.g., Cottrell et al., 2021), with the lherzolite samples showing a wide range of fO_2 from 0.28 to 1.18 log units (ΔFMQ). The moderate degree of melt extraction estimated for the Hyblean peridotites (up to ~17%, estimated by spinel Cr# in Fig. S11, and both Y and Yb in clinopyroxene by Perinelli et al. (2008)) is in agreement with the global distribution of abyssal peridotites collected from mid-oceanic ridges (Warren, 2016). The Fe^{3+} of the bulk rock is expected to be roughly constant according to the model proposed by Gaetani (2016). However, Fig. 7a shows that Hyblean peridotites are more oxidized than either modern MORBs or abyssal peridotites, while overlap with fO_2 typical of arc peridotites and spinel peridotite xenoliths ($-1 <$ logfO_2 (ΔFMQ) < 2, Ballhaus, 1993; Cottrell et al., 2021). Fig. 7a includes a reference buffer representing the equilibrium between graphite and C-O-H fluids with variable composition (Ulmer and Luth, 1991) calculated along a geotherm of ~70 mW·m^{-2} (Perinelli et al., 2008). Hyblean peridotites fall above the C-COH buffer (i.e., C-O-H fluids field; Fig. 7a), suggesting that any (metasomatic) oxidized fluid interacting with the crystalline matrix is thermodynamically stable. The diagram logfO_2 (ΔFMQ) versus $Fe^{3+}/\sum Fe_{spinel}$ (Fig. 6) can be used to estimate how much Fe is oxidized from Fe^{2+} to Fe^{3+} to increase the fO_2 by 1 log unit. In the case of the Hyblean samples, an increase of $Fe^{3+}/\sum Fe$ by about 10% is needed to increase the logfO_2 from conditions where graphite would be stable to the currently estimated redox conditions.

In this view, pyroxenites/websterites recovered along with peridotite xenoliths in the Valle Guffari diatreme (Nimis and Vannucci, 1995) and interpreted as products of polybaric, high-pressure fractional crystallization of tholeiitic to alkaline primitive magmas, provide a scenario for the lithospheric mantle beneath the Hyblean Plateau that can be seen in terms of gradual and continuous oxidation and refertilization. This scenario is also supported by the geochemical and isotopic signatures of Hyblean Plateau basalts formed from a mantle source metasomatized by small degrees of partial melts rich in CO_2 (Trua et al., 1998). Therefore, if, on one hand, the extraction of both alkaline (ocean island basalt (OIB)-like) and tholeiitic (MORB-like) magmas could have contributed to leaving behind a residual Fe^{3+}-depleted mantle source, the persistent interaction with (subduction-related) metasomatic fluids acted towards an increase of the local redox state of the lithospheric mantle underneath the Hyblean Plateau. As a reference value, taken into account the partitioning behavior of the ferric iron during partial melting of a spinel peridotite (Sorbadere et al., 2018), seafloor abyssal peridotites can represent the reduced lithospheric mantle after extensive melt extraction having logfO_2 ranging from −2 to 0 log units (ΔFMQ; Bryndzia and Wood, 1990; Birner et al., 2018), while spinel peridotite xenoliths are more oxidized above FMQ as result of the metasomatism (Ballhaus, 1993). Our samples show the $Fe^{3+}/\Sigma Fe$ in spinel varying between 0.30 and 0.35 that is higher than in spinels from reduced residual peridotites, with consequent high fO_2 conditions, as shown in Fig. 6 and 7, suggesting the interaction through time with oxidized fluids, some of which were sampled as inclusions by the silicate minerals analyzed in this and previous studies (e.g., Sapienza et al., 2005). By plotting the calculated logfO_2 (ΔFMQ) as a function of the spinel Cr# as proposed by Ballhaus et al. (1991), further evidence of the interaction between the Hyblean samples and metasomatic fluids is shown in Fig. 12, where Hyblean samples fall in the field of slightly metasomatized xenoliths along with Vitim off-craton metasomatized spinel-peridotites (Goncharov and Ionov, 2012). Moreover, Perinelli et al. (2008) observed an increase of spinel TiO_2 wt% at constant Cr#, attributed to the reaction with a metasomatic source. Interestingly, all the samples, both lherzolites and harzburgites, do not deviate from the Olivine-Spinel Mantle Array (OSMA; Arai, 1994) as shown in Fig. S11 of the Supplementary Materials ($Cr\#_{spinel}$ versus $Mg\#_{olivine}$). Therefore, spinel Cr# was probably controlled by both partial melting processes and interaction with metasomatic agents that did not carry significant Mg/Fe.

4.2. *Chemical composition and origin of metasomatic volatile-bearing melts trapped in silicate minerals*

The reconstruction of redox features for the potential metasomatic agent(s) in the studied xenoliths relies on thermodynamic models such as Zhang and Duan (2009) that allow mostly to constrain the molar

fraction of H_2O versus CO_2 species as a function of P, T and fO_2 within the simplified C-O-H chemical system. However, these calculations require the integration with the accurate characterization of fluid inclusions as those trapped in the silicate minerals of the Hyblean spinel-peridotites. It is noteworthy that the inclusions described by Sapienza et al. (2005) and Correale et al. (2012, 2015) on a similar suite of peridotite xenoliths from Valle Guffari appeared highly CO_2-rich (up to 11–11.5 $\cdot 10^{-7}$ mol·gr^{-1} in sample XIH-3 of Correale et al., 2015) and contained rare minerals reported to be magnesite and anhydrite (Sapienza et al., 2005). The inclusions analyzed in olivines from samples VG14 and VG36 confirm the dominance of carbonates and CO_2 in the inclusions coexisting with several S-bearing phases (see Figs. 8a-f) and (secondary) hydrous phases. More in detail, we observed the coexistence of carbonate and sulfate in the most oxidized sample VG36, and carbonate, native sulfur, and sulfide in the reduced sample VG14. The preliminary analyses on inclusions in coexisting opx and cpx confirm previous observations of CO_2 being the dominant phase. No evidence of silicate minerals is reported other than serpentine.

Nevertheless, some of the inclusions in VG14 and VG36 were observed to originate from glass microveins (Fig. 2b), suggesting an injection of a metasomatic melt. We noted similarities with the composition of the fluid inclusions described by Sandoval-Velasquez et al. (2021a) in mantle xenoliths from the Mexico subduction zone, where the coexistence of carbonate and CO_2, as well as carbonate (magnesite) and sulfide (pyrite), was reported. S-rich inclusions in mantle xenoliths were also previously detected in Canary Island xenoliths (Bodnar and Frezzotti, 2020; Oglialoro et al., 2017), where a subduction-related component in the mantle was assumed (Sandoval-Velasquez et al., 2021b).

The inclusions analyzed by Sapienza et al. (2005) in pyroxene and olivine are almost pure CO_2 plus rare findings of magnesite that the authors explain as likely formed by reaction with the host wall and anhydrite. These inclusions were proposed to represent a snapshot of the CO_2 exsolution by decompression from a metasomatic silicate melt during its upward migration. Microthermometric measurements fixed a minimum depth of entrapment of these fluids at about 1.1 GPa (~41 km). The study carried out by Correale et al. (2015) on CO_2 fluid inclusions of Hyblean pyroxenes helped to clarify the contribution of C from a deeper subduction-related source for the origin of the CO_2 trapped in pyroxenes both of peridotites and pyroxenites resulting into an isotopic variability ($-4 < \delta^{13}C$ versus PDB < -2 measured in the case of the peridotitic sample). The carbonate-CO_2-rich nature of the inclusions measured in this study, coupled with the C isotopic signature of the inclusions in Valle Guffari xenoliths reported by Correale et al. (2015), require, therefore, the involvement of CO_2-rich metasomatic agents, the composition of which might be represented by near-solidus carbonatitic melts that, while moving upward, experienced crystallization and volatile exsolution upon decompression/cooling. Importantly, the finding of (silicate) glass microveins in our VG14 and VG36 samples implies a compositional evolution of the metasomatic melt towards a more SiO_2-rich component. Scribano et al. (2009) describe harzburgitic samples from the same area characterized by the coexistence of rare dolomitic globules with silicate glass all surrounding amphiboles (pargasite) of metasomatic origin. This event must be temporarily distinct as we did not observe in our samples either carbonate globules or amphibole/phlogopite minerals typical of modal metasomatism. However, we observed the replacement of opx by jadeitic-rich cpx (Na_2O content varying from 0.37 to 1.54; see Table S1c of the Supplementary Materials) coexisting with (secondary) low-Al opx, which resembles that described by Yaxley et al. (1991); see Table 1) for spinel peridotite xenoliths from Western Victoria (Australia) with geochemical evidence of interaction with Na-bearing CO_2-rich metasomatic melts. Moreover, an increase of CaO/Al_2O_3 of the bulk rock was observed, ranging from 1.10 to 1.40, higher than the 0.95 expected for average subcontinental spinel lherzolites (McDonough, 1990). In addition, the non-primary nature of the cpx is supported by its Cr_2O_3 content in correlation with Na_2O (Dawson, 2002). The absence of hydrous Na-bearing minerals in our samples might be related to the low Na content of a dry metasomatic melt, sufficient only to increase the jadeitic content of cpx. A recent study (El Dien et al., 2019) pointed out the role of spl in revealing the interaction with fluids by looking at the variation of Cr_2O_3 and Al_2O_3 between single grains core and rim. The slight variation observed in the Hyblean lherzolitic spinels, controlled by both metasomatism and partial melting as proposed by El Dien et al. (2019; Figure S12 of the Supplementary Materials) coupled with enrichment in Na_2O of cpx and decrease of Al_2O_3 of the bulk rock, suggests the interaction with small amounts of metasomatic melts through time, which likely started deeper in the lithosphere. The persistency of this interaction can explain the low chemical differences between core and rim resulting from the prolonged cation diffusion between fluid and spinel. By similarity, the inclusions trapped in our samples also contain Na-bearing minerals (glauberite, thenardite and burkeite) that, along with the frequent carbonate minerals and the rare silicate veins, can be ascribed to daughter minerals forming from Na-bearing carbonatitic to carbonate-silicate (metasomatic) melts. There is no geochemical evidence that modal metasomatism (Scribano et al., 2009), cryptic metasomatism (Perinelli et al., 2008), metasomatism recorded by cpx and opx CO_2-rich inclusions (Correale et al., 2015; Sapienza et al., 2005) and that recorded by inclusions in olivines from VG14 and VG36 (this study) are related to the same metasomatic stage or distinct events. However, the mineral assemblage and the carbonated nature of the inclusions in olivine, along with the enrichment in Na_2O of cpx indicate that all the metasomatic agents likely originated from the same deep source. Na-bearing CO_2-rich liquids generally refer to products of low-degree partial melting of carbonated eclogites experimentally quenched at variable pressures and temperatures coexisting with an immiscible, more silica-rich melt (Dasgupta et al., 2004, 2006; Hammouda, 2003; Stagno et al., 2015). Although the chemical composition of the segregated melts is strongly controlled by the chemical composition of the source rock, Thomson et al. (2016) pointed out the positive effect of pressure in stabilizing carbonatitic melts with an increasing amount of Na_2O from <1 wt% at P below 7 GPa up to ~4.5 wt% at about 15 GPa. Na-rich carbonatites (Na_2O up to 15 wt%) were proposed to form at depths near the bottom of the upper mantle (~ 21 GPa). Therefore, we conclude that fluid inclusions trapped in olivine crystals from VG14 and VG36, along with the petrographic and geochemical evidence of modal metasomatism previously reported (Scribano et al., 2009), might both record a metasomatic melt with a deep origin that is chemically distinct from that recorded in cpx (and opx) grains from Sapienza et al. (2005) and Correale et al. (2012), where Na-rich daughter minerals in fluid inclusions were not detected.

Further, the Raman micro-analysis on olivine inclusions revealed the presence of S in different oxidation states, S^0 (native sulfur) and S^{2-} (sulfide) in VG14, and S^{6+} (sulfates) in VG36, coexisting with carbonates. First, recent experimental studies have shown that the solubility of S in carbonatitic to carbonate-silicate melts is limited to <0.5 wt% when coexisting with a sulfide mineral (Chowdhury and Dasgupta, 2020) or a sulfide liquid (Stagno and Frost, 2010). An origin of S-bearing minerals from carbonatitic or carbonate-silicate melts is supported by optical observations of the analyzed inclusions, showing that S-minerals are volumetrically much smaller than the CO_2-rich portion. Alternatively, the origin of these S- daughter minerals might rely on the remobilization of S from primary sulfides from the host peridotite by permeating metasomatic melts. Indeed, the mineralogy of some of the daughter minerals matches the composition of sulfides from the Hyblean peridotites (Sapienza et al., 2007). However, the occurrence of primary sulfides remains debated as most of these S minerals have been proposed to be the product of serpentinization (Scribano et al., 2009).

The intrinsic redox state of the metasomatic fluid/melt has the main control on the speciation of S as sulfide, native sulfur, or sulfate in the inclusions. In particular, thermodynamic predictions of the coexistence of sulfides and sulfates (SST line in Fig. 7a) as a function of the fO_2

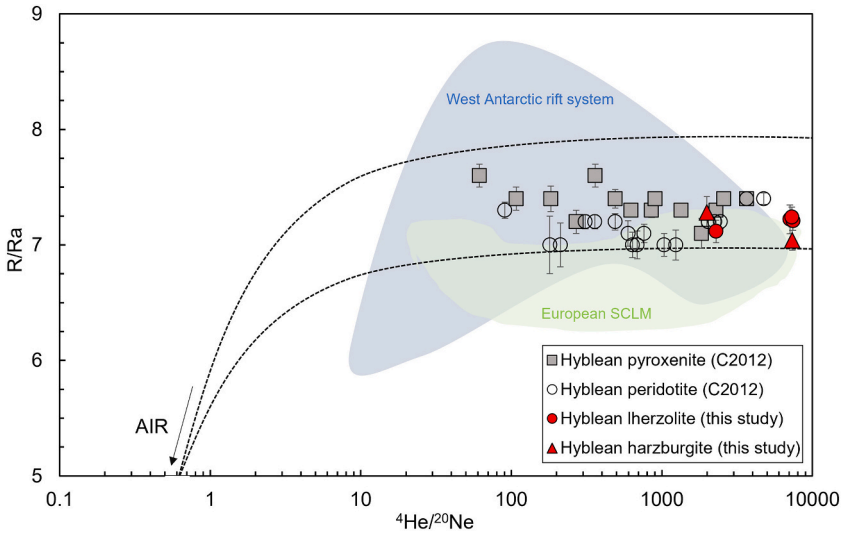

Fig. 13. R/Ra ratio vs ^{4}He/^{20}Ne for Hyblean spinel-peridotites (this study) and spinel-peridotites and pyroxenites from Correale et al. (2012). Black lines represent the mixing between air and an upper mantle source with R/Ra values between 7 and 8 from Sandoval-Velasquez et al. (2021a). The field of the European SCLM in blue and the West Antarctic Rift System are reported according to Sandoval-Velasquez et al., 2021aand references therein. (For interpretation of the references to colour in this figure legend, the reader is referred to the web version of this article.)

indicate values ranging between 0 log units at 1 GPa and 1.8 at 8 GPa (Chowdhury and Dasgupta, 2020). The logfO_2 (ΔFMQ) of sample VG14 (0.32 log units) is quite close to the SST line and might explain why native S and sulfides are found to coexist; while VG36 is more oxidized (1.27 log units) well above the SST line, hence, explaining the speciation of S as sulfate. On the other hand, Na-bearing CO_2-rich melts are characterized by low viscosity and high mobility (Stagno et al., 2018; Stagno et al., 2020), other than being extremely reactive with the surrounding crystalline matrix. The preservation of the oxidation state of redox-sensitive elements like S must depend on the local fO_2 of the host rock. As mentioned above, a residual peridotite with initial logfO_2 (ΔFMQ) between −2 and 0 must have experienced a significant oxidation event to record the fO_2 values determined in our samples. Whether such oxidation occurred as a single event or at multiple stages would have depended on the melt/rock ratio and, in turn, the kinetics of interaction between metasomatic melt and minerals. On the other hand, the diverse chemical composition of the fluid inclusions from Hyblean xenoliths (from pure CO_2 fluids to Na-, S-bearing carbonate liquids; Sapienza et al., 2005; Correale et al., 2012; this study) supports the possibility that such oxidation occurred at subsequent stages (e.g., multiple melt injections).

4.3. Noble gases signature

Considering that Hyblean lithospheric mantle rocks record multiple metasomatic events likely variable in terms of the chemical composition of the interacting fluids/melts, the study of noble gases from the selected single crystals of known chemical composition and analyzed inclusions can help to retrieve additional information about the source of the metasomatic agents. In fact, the C and He systematic in the Hyblean xenoliths indicates 1) the occurrence of mixing between a MORB (pyroxenites) and a HIMU (peridotite) mantle end members and 2) a crustal C component (organic and sedimentary) in the mantle (Correale et al., 2012, 2015). However, the diagram R/Ra versus ^{4}He/^{20}Ne (Fig. 13) shows values that fall along the air-mantle mixing curve and overlap with those measured in mantle xenoliths from the European SCLM and the West Antarctic Rift System (Sandoval-Velasquez et al., 2021a and references therein). Furthermore, the atmospheric contribution with respect to the mantle contribution is also supported by the relationship ^{4}He/^{20}Ne ratio versus the ^{40}Ar/^{36}Ar ratio (Fig. 10). Here, two samples (lherzolite VG24 and harzburgite VG29) have ^{40}Ar/^{36}Ar up to 1590 that indicate a higher mantle contribution compared to literature data (Correale et al., 2012) and both these samples have a He/^{40}Ar* (1.28–1.42) in the typical range of the mantle value (^{4}He/^{40}Ar* = 1–5;

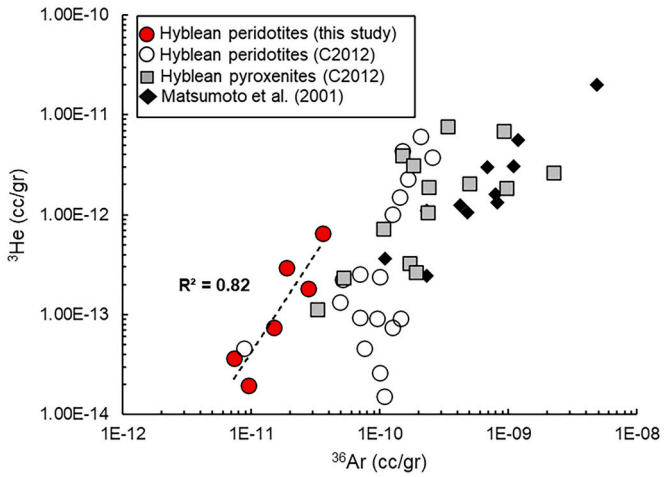

Fig. 14. (a) Concentration of ^{3}He plotted as function ^{36}Ar for Hyblean olivine along with Matsumoto et al. (2001) and Correale et al. (2012) data. R^2 of the linear fit line for samples from this study is reported.

Yamamoto et al., 2009; Marty, 2012), as shown in Fig. 11. We also observed a positive relation between ^{3}He (a mantle component) and ^{36}Ar (an atmospheric component; Fig. 14) as previously recorded in mantle xenoliths (Matsumoto et al., 2001; Sandoval-Velasquez et al., 2021a), suggesting that a possible deep origin of the atmospheric component could also be considered. This is also supported by the petrological considerations on the metasomatic agents discussed in the previous sections, e.g., the high redox conditions comparable with that of arc peridotites (Cottrell et al., 2021), the composition of the analyzed inclusions in olivine (S-rich) similar to those retrieved in samples where a recycled crustal component was identified (Bodnar and Frezzotti, 2020; Oglialoro et al., 2017; Sandoval-Velasquez et al., 2021a, 2021b) and the evidence of interaction with a Na-bearing CO_2-rich melt (Yaxley et al., 1991), which can originate from the partial melting of a carbonated eclogite (Dasgupta et al., 2004, 2006; Hammouda, 2003; Stagno et al., 2015). Moreover, the δ^{13}C by Correale et al. (2015) on Hyblean xenoliths (same samples as Correale et al., 2012) showed values for fluid inclusions compatible with a (slab-related) contamination by sedimentary and organic C. Therefore, considering all these, we cannot exclude that an atmospheric component identified in the fluid inclusions can also be related to the atmosphere recycled in the upper mantle through subduction.

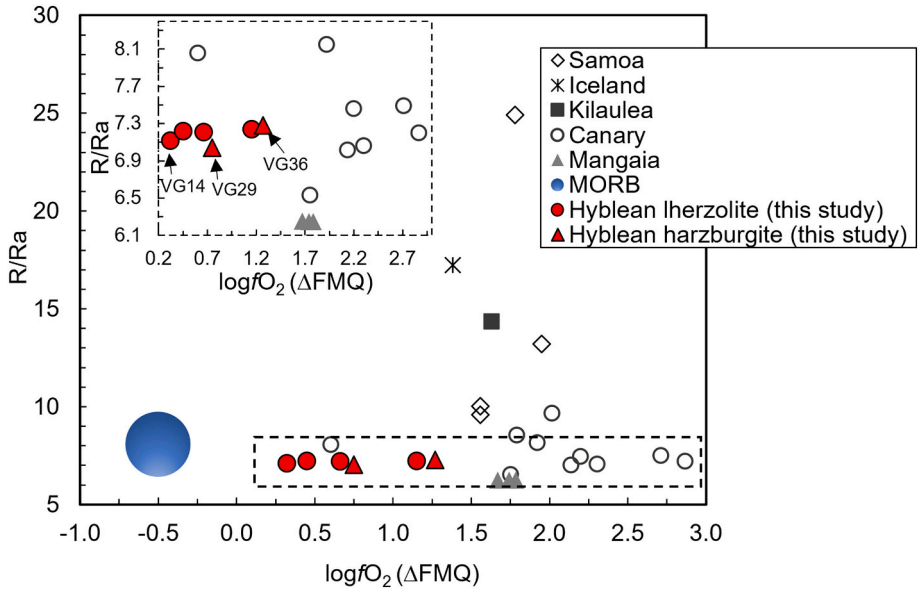

Fig. 15. R/Ra plotted as a function of logfO_2 (ΔFMQ) for literature OIBs (Day et al., 2022 and references therein) and Hyblean spinel-peridotites. The dashed area is a zoom on the Hyblean samples field, where lherzolite VG14 and harzburgite VG36 are indicated with arrows along with the most serpentinized sample, lherzolite VG29.

We also assess the contribution of an oxidized slab component by comparing logfO_2 and R/Ra of the Hyblean peridotites, with respect to the well-constrained MORB (R/Ra = 8 ± 1 and logfO_2 of −0.5; Day et al., 2022 and references therein), if the crustal ^{4}He component is strong enough to decrease the He isotopic signature down to the typical mantle values (e.g., MORB 8 ± 1; Graham, 2002). This is reported in Fig. 15 along with literature data relative to plume-related OIBs such as those from Iceland, Samoa, Kilauea and Mangaia and with Canary OIBs with a typical MORB-like isotopic signature (Day et al., 2022 and references therein). Harzburgitic samples are those with R/Ra of 7.04 (VG29) and 7.28 (VG36). Samples VG14 and VG36 are indicated by arrows. A sample (VG29) shows higher serpentinization than the other samples and is also indicated. An optimistic linear correlation of R/Ra versus logfO_2 (ΔFMQ) would imply a direct contribution of the crustal component to the oxidizing effect of metasomatism but, when the uncertainties on the R/Ra are considered, the data appear randomly distributed, as in the case of samples that were distinctly contaminated through time. However, Hyblean peridotites are also linked to a HIMU-type mantle source (Correale et al., 2012 and this study) with He isotopic signature lower than the MORB values suggesting the presence of recycled crustal materials.

5. Conclusions

In this study, we investigated eight spinel-peridotites nodules from Valle Guffari (Sicily) to reconstruct the origin of the metasomatism of the Hyblean Plateau mantle, previously reported in the literature but still debated, and its redox evolution. A multidisciplinary approach was employed, combining Fe^{3+} measurements in spinel and oxy-thermobarometric fO_2 estimations with chemical characterization of fluid inclusions in olivine through micro-Raman and micro-FTIR and noble gases measurements.

These samples are more oxidized than other peridotitic suites worldwide distributed from cratonic and abyssal peridotites, with logfO_2 (ΔFMQ) estimated to range between 0.28 and 1.27, overlapping values for arc peridotites and falling in the lightly metasomatized xenoliths field (logfO_2 vs Cr#) as proposed by Ballhaus et al. (1991). Coexisting fluids are predicted to be thermodynamically stable in the form of CO_2 and H_2O at these redox conditions. Direct evidence of interaction with metasomatic melts is represented by the occurrence of silicate glass microveins from which multiple trails of fluid/mineral inclusions originate. The fluid inclusions contain an assemblage of Mg-Ca carbonates ± sulfide ± sulfur ± CO_2 for the reduced sample VG14 (0.32 log units) and Mg-Ca carbonates ± Na-rich sulfates ± CO_2 for the most oxidized sample VG36 (1.27 log units), suggesting Na-bearing carbonatitic to carbonate-silicate melts as possible metasomatic agents. The slight chemical heterogeneity from the core to the rim of spinels (Cr_2O_3 vs Al_2O_3) coupled with the high logfO_2 (a negligible variation is observed between core and rim) recorded with respect to the ambient lithospheric mantle (−2 to 0 log units) are interpreted as the result of a significant oxidation event that could have happened all at once or intermittently mainly depending on the melt/rock ratio, although the diverse chemical composition of the fluid inclusions would support multistage metasomatism. The systematics of noble gases (He, Ar, Ne), supported by the high registered redox conditions, the geochemical evidence of interaction with Na-CO_2-rich melts, the chemical composition of the analyzed inclusions (C-S-Na-rich), and the previous isotopic evidence of sedimentary and organic C component in Hyblean peridotitic mantle (Correale et al., 2015), indicate the contribution of a slab-derived component in fluid trapped in olivines. Combining all data, we conclude that the lithospheric mantle beneath the Hyblean Plateau, through time, experienced interactions with metasomatic subduction-related (deep) CO_2-rich silicate-bearing melts.

Declaration of Competing Interest

The authors declare that they have no known competing financial interests or personal relationships that could have appeared to influence the work reported in this paper.

Acknowledgements

V.S. gratefully acknowledges “Fondi di Ateneo 2021” provided by Sapienza University, the support from the European Synchrotron Radiation Facility for the provision of beam time at ID18 Nuclear Resonance Beamline, and Elettra synchrotron Trieste for provision beam time at beamline SISSI-Mat Science. Raman facilities at Milano Bicocca were provided by the Department of Earth and Environmental Sciences within the frame of the Milano Bicocca spectroscopy network. A.C. appreciates support by the “Ramón y Cajal” research program (RYC2021-033270-I;

MCIN/AEI/10.13039/501100011033 - EU "NextGenerationEU/PRTR). Maria Grazia Minisseri is acknowledged for contributing to the noble gases analysis at the INGV laboratory. The authors greatly acknowledge Domenico Mannetta for the preparation of double-polished thin sections and Marco Albano, Tania Ruspandini and Marcello Serracino for helping with SEM and EPMA facilities. We acknowledge thoughtful and constructive comments from Suzanne Birner and an anonymous reviewer.

Appendix A. Supplementary data

Supplementary data to this article can be found online at https://doi.org/10.1016/j.lithos.2023.107337.

References

Arai, S., 1994. Characterization of spinel peridotites by olivine-spinel compositional relationships: review and interpretation. Chem. Geol. 113 (3–4), 191–204.
Ballhaus, C., 1993. Redox states of lithospheric and asthenospheric upper mantle. Contrib. Mineral. Petrol. 114 (3), 331–348.
Ballhaus, C., Berry, R.F., Green, D.H., 1991. High pressure experimental calibration of the olivine-orthopyroxene-spinel oxygen geobarometer: implications for the oxidation state of the upper mantle. Contrib. Mineral. Petrol. 107, 27–40.
Beccaluva, L., Siena, F., Coltorti, M., Grande, A.D., Giudice, A.L., Macciotta, G., Vaccaro, C., 1998. Nephelinitic to tholeiitic magma generation in a transtensional tectonic setting: an integrated model for the Iblean volcanism, Sicily. J. Petrol. 39 (9), 1547–1576.
Birner, S.K., Cottrell, E., Warren, J.M., Kelley, K.A., Davis, F.A., 2018. Peridotites and basalts reveal broad congruence between two independent records of mantle fO_2 despite local redox heterogeneity. Earth Planet. Sci. Lett. 494, 172–189.
Birner, S.K., Cottrell, E., Warren, J.M., Kelley, K.A., Davis, F.A., 2021. Melt addition to mid-ocean ridge peridotites increases spinel Cr# with no significant effect on recorded oxygen fugacity. Earth Planet. Sci. Lett. 566, 116951.
Bodnar, R.J., Frezzotti, M.L., 2020. Microscale chemistry: Raman analysis of fluid and melt inclusions. Elements 16, 93–98.
Brey, G.P., Köhler, T.P., 1990. Geothermometry in four-phase lherzolites II: new thermobarometers, and practical assessment of existing thermobarometers. J. Petrol. 31, 1353–1378.
Bryndzia, L.T., Wood, B.J., 1990. Oxygen thermobarometry of abyssal spinel peridotites: the redox state and COH volatile composition of the Earth's sub-oceanic upper mantle. Am. J. Sci. (USA) 290 (10).
Canil, D., O' Neill, H.S.tC., 1996. Distribution of ferric iron in some upper-mantle assemblages. J. Petrol. 37, 609–635.
Chowdhury, P., Dasgupta, R., 2020. Sulfur extraction via carbonated melts from sulfide-bearing mantle lithologies–implications for deep sulfur cycle and mantle redox. Geochim. Cosmochim. Acta 269, 376–397.
Correale, A., Martelli, M., Paonita, A., Rizzo, A., Brusca, L., Scribano, V., 2012. New evidence of mantle heterogeneity beneath the Hyblean Plateau (Southeast Sicily, Italy) as inferred from noble gases and geochemistry of ultramafic xenoliths. Lithos 132, 70–81.
Correale, A., Paonita, A., Rizzo, A., Grassa, F., Martelli, M., 2015. The carbon-isotope signature of ultramafic xenoliths from the Hyblean Plateau (Southeast Sicily, Italy): evidence of mantle heterogeneity. Geochem. Geophys. Geosyst. 16 (3), 600–611.
Cottrell, E., Birner, S.K., Brounce, M., Davis, F.A., Waters, L.E., Kelley, K.A., 2021. Oxygen fugacity across tectonic settings. Magma Redox Geochem. 33–61.
Cristofolini, R., 1966. Lemanifestazioni eruttive basiche del trias superiore nel sottosuolo di Ragusa (Sicilia sud-orientale). Period. Mineral. 35, 1–28.
Dasgupta, R., Hirschmann, M.M., Withers, A.C., 2004. Deep global cycling of carbon constrained by the solidus of anhydrous, carbonated eclogite under upper mantle conditions. Earth Planet. Sci. Lett. 227 (1–2), 73–85.
Dasgupta, R., Hirschmann, M.M., Stalker, K., 2006. Immiscible transition from carbonate-rich to silicate-rich melts in the 3 GPa melting interval of eclogite+ CO_2 and genesis of silica-undersaturated ocean island lavas. J. Petrol. 47 (4), 647–671.
Dawson, J.B., 2002. Metasomatism and partial melting in upper-mantle peridotite xenoliths from the Lashaine volcano, northern Tanzania. J. Petrol. 43 (9), 1749–1777.
Day, J.M., Jones, T.D., Nicklas, R.W., 2022. Mantle sources of ocean islands basalts revealed from noble gas isotope systematics. Chem. Geol. 587, 120626.
De Grave, E., Van Alboom, A., 1991. Evaluation of ferrous and ferric Mössbauer fractions. Phys. Chem. Miner. 18 (5), 337–342.
El Dien, H., Arai, S., Doucet, L.S., Li, Z.X., Kil, Y., Fougerouse, D., Reddy, S., Saxey, D.W., Hamdy, M., 2019. Cr-spinel records metasomatism not petrogenesis of mantle rocks. Nat. Commun. 10 (1), 1–12.
Frezzotti, M.L., Peccerillo, A., 2007. Diamond-bearing COHS fluids in the mantle beneath Hawaii. Earth Planet. Sci. Lett. 262 (1–2), 273–283.
Frezzotti, M.L., Tecce, F., Casagli, A., 2012a. Raman spectroscopy for fluid inclusion analysis. J. Geochem. Explor. 112, 1–20.
Frezzotti, M.L., Ferrando, S., Tecce, F., Castelli, D., 2012b. Water content and nature of solutes in shallow-mantle fluids from fluid inclusions. Earth Planet. Sci. Lett. 351, 70–83.
Frost, D.J., McCammon, C.A., 2008. The redox state of Earth's mantle. Annu. Rev. Earth Planet. Sci. 36, 389–420.
Gaetani, G.A., 2016. The behavior of $Fe^{3+}/\sum$ Fe during partial melting of spinel lherzolite. Geochim. Cosmochim. Acta 185, 64–77.
Goncharov, A.G., Ionov, D.A., 2012. Redox state of deep off-craton lithospheric mantle: new data from garnet and spinel peridotites from Vitim, southern Siberia. Contrib. Mineral. Petrol. 164 (5), 731–745.
Goncharov, A.G., Ionov, D.A., Doucet, L.S., Pokhilenko, L.N., 2012. Thermal state, oxygen fugacity and C-O-H fluid speciation in cratonic lithospheric mantle: new data on peridotite xenoliths from the Udachnaya kimberlite, Siberia. Earth Planet. Sci. Lett. 357, 99–110.
Graham, D.W., 2002. Noble gas isotope geochemistry of mid-ocean ridge and ocean island basalts: characterization of mantle source reservoirs. Rev. Mineral. Geochem. 47, 247–319.
Hammouda, T., 2003. High-pressure melting of carbonated eclogite and experimental constraints on carbon recycling and storage in the mantle. Earth Planet. Sci. Lett. 214 (1–2), 357–368.
Hellebrand, E., Snow, J.E., Dick, H.J., Hofmann, A.W., 2001. Coupled major and trace elements as indicators of the extent of melting in mid-ocean-ridge peridotites. Nature 410 (6829), 677–681.
Jianping, L., Kornprobst, J., Vielzeuf, D., Fabriès, J., 1995. An improved experimental calibration of the olivine-spinel geothermometer. Chin. J. Geochem. 14, 68–77.
Klemme, S., 2004. The influence of Cr on the garnet–spinel transition in the Earth's mantle: experiments in the system $MgO–Cr_2O_3–SiO_2$ and thermodynamic modelling. Lithos 77 (1–4), 639–646.
Köhler, T.P., Brey, G., 1990. Calcium exchange between olivine and clinopyroxene calibrated as a geothermobarometer for natural peridotites from 2 to 60 kb with applications. Geochim. Cosmochim. Acta 54 (9), 2375–2388.
MacGregor, I.D., 2015. Empirical geothermometers and geothermobarometers for spinel peridotite phase assemblages. Int. Geol. Rev. 57 (15), 1940–1974.
Marras, G., Carnevale, G., Caracausi, A., Rotolo, S.G., Stagno, V., 2023. First measurements of the Fe oxidation state of spinel inclusions in olivine single crystals from Vulture (Italy) with the in situ synchrotron micro-Mössbauer technique. Europ. J. Mineral. 35 (4), 665–678.
Martin, A.P., Price, R.C., Cooper, A.F., McCammon, C.A., 2015. Petrogenesis of the rifted southern Victoria Land lithospheric mantle, Antarctica, inferred from petrography, geochemistry, thermobarometry and oxybarometry of peridotite and pyroxenite xenoliths from the Mount Morning eruptive Centre. J. Petrol. 56 (1), 193–226.
Marty, B., 2012. The origins and concentrations of water, carbon, nitrogen and noble gases on Earth. Earth Planet. Sci. Lett. 313, 56–66.
Marty, B., Zashu, S., Ozima, M., 1983. Two noble gas components in a Mid-Atlantic Ridge basalt. Nature 302, 238–240.
Matsumoto, T., Chen, Y., Matsuda, J.I., 2001. Concomitant occurrence of primordial and recycled noble gases in the Earth's mantle. Earth Planet. Sci. Lett. 185 (1–2), 35–47.
McCammon, C., Kopylova, M.G., 2004. A redox profile of the Slave mantle and oxygen fugacity control in the cratonic mantle. Contrib. Mineral. Petrol. 148 (1), 55–68.
McDonough, W.S., 1990. Constraints on the composition of the continental lithospheric mantle. Earth Planet. Sci. Lett. 101 (1), 1–18.
Miller, W.G., Holland, T.J., Gibson, S.A., 2016. Garnet and spinel oxybarometers: new internally consistent multi-equilibria models with applications to the oxidation state of the lithospheric mantle. J. Petrol. 57 (6), 1199–1222.
Nimis, P., 1998. Clinopyroxene geobarometry of pyroxenitic xenoliths from Hyblean Plateau (SE Sicily, Italy). Eur. J. Mineral. 10, 521–534.
Nimis, P., Grütter, H., 2010. Internally consistent geothermometers for garnet peridotites and pyroxenites. Contrib. Mineral. Petrol. 159, 411–427.
Nimis, P., Vannucci, R., 1995. An ion microprobe study of clinopyroxenes in websteritic and megacrystic xenoliths from Hyblean Plateau (SE Sicily, Italy): constraints on HFSE/REE/Sr fractionation at mantle depth. Chem. Geol. 124 (3–4), 185–197.
Nuccio, P.M., Paonita, A., Rizzo, A., Rosciglione, A., 2008. Elemental and isotope covariation of noble gases in mineral phases from Etnean volcanics erupted during 2001–2005, and genetic relation with peripheral gas discharges. Earth Planet. Sci. Lett. 272 (3–4), 683–690.
Oglialoro, E., Frezzotti, M.L., Ferrando, S., Tiraboschi, C., Principe, C., Groppelli, G., Villa, I.M., 2017. Lithospheric magma dynamics beneath the El Hierro Volcano, Canary Islands: insights from fluid inclusions. Bull. Volcanol. 79 (10), 1–17.
O'Neill, H.S.C., 1981. The transition between spinel lherzolite and garnet lherzolite, and its use as a geobarometer. Contrib. Mineral. Petrol. 77, 185–194.
Perinelli, C., Sapienza, G.T., Armienti, P., Morten, L., 2008. Metasomatism of the upper mantle beneath the Hyblean Plateau (Sicily): evidence from pyroxenes and glass in peridotite xenoliths. Geol. Soc. Lond., Spec. Publ. 293, 197–221.
Perinelli, C., Andreozzi, G.B., Conte, A.M., Oberti, R., Armienti, P., 2012. Redox state of subcontinental lithospheric mantle and relationships with metasomatism: insights from spinel peridotites from northern Victoria Land (Antarctica). Contrib. Mineral. Petrol. 164 (6), 1053–1067.
Perinelli, C., Bosi, F., Andreozzi, G.B., Conte, A.M., Armienti, P., 2014. Geothermometric study of Cr-spinels of peridotite mantle xenoliths from northern Victoria Land (Antarctica). Am. Mineral. 99 (4), 839–846.
Potapkin, V., Chumakov, A.I., Smirnov, G.V., Celse, J.P., Rüffer, R., McCammon, C., Dubrovinsky, L., 2012. The ^{57}Fe Synchrotron Mössbauer source at the ESRF. J. Synchrotron Radiat. 19, 559–569.
Prescher, C., McCammon, C.A., Dubrovinsky, L., 2012. MossA: a program for analyzing energy-domain Mössbauer spectra from conventional and synchrotron sources. J. Appl. Crystallogr. 45, 329–331.
Rizzo, A.L., Pelorosso, B., Coltorti, M., Ntaflos, T., Bonadiman, C., Matusiak-Małek, M., Italiano, F., Bergonzoni, G., 2018. Geochemistry of noble gases and CO_2 in fluid

inclusions from lithospheric mantle beneath wilcza góra (lower silesia, Southwest Poland). Front. Earth Sci. 6, 215. https://doi.org/10.3389/feart.2018.00215.
Sandoval-Velasquez, A., Rizzo, A.L., Frezzotti, M.L., Saucedo, R., Aiuppa, A., 2021a. The composition of fluids stored in the central Mexican lithospheric mantle: inferences from noble gases and CO2 in mantle xenoliths. Chem. Geol. 576, 120270.
Sandoval-Velasquez, A., Rizzo, A.L., Aiuppa, A., Remigi, S., Padron, E., Perez, N.M., Frezzotti, M.L., 2021b. Recycled crustal carbon in the depleted mantle source of El Hierro volcano, Canary Islands. Lithos 400, 106414.
Sapienza, G., Scribano, V., 2000. Distribution and representative whole-rock chemistry of deep-seated xenoliths from the Iblean Plateau, South-Eastern Sicily, Italy. Period. Mineral. 69, 185–204.
Sapienza, G., Hilton, D.R., Scribano, V., 2005. Helium isotopes in peridotite mineral phases from Hyblean Plateau xenoliths (South-Eastern Sicily, Italy). Chem. Geol. 219 (1–4), 115–129.
Sapienza, G.T., Griffin, W.L., O'Reilly, S.Y., Morten, L., 2007. Crustal zircons and mantle sulfides: Archean to Triassic events in the lithosphere beneath South-Eastern Sicily. Lithos 96 (3–4), 503–523.
Scribano, V., Carbone, S., 2020. Convective instability in intraplate oceanic mantle caused by Amphibolite-derived Garnet-Pyroxenites—a Xenolith perspective (Hyblean Plateau, Sicily). Geosciences 10 (9), 378.
Scribano, V., Viccaro, M., Cristofolini, R., Ottolini, L., 2009. Metasomatic events recorded in ultramafic xenoliths from the Hyblean area (Southeastern Sicily, Italy). Mineral. Petrol. 95 (3), 235–250.
Sorbadere, F., Laurenz, V., Frost, D.J., Wenz, M., Rosenthal, A., McCammon, C., Rivard, C., 2018. The behaviour of ferric iron during partial melting of peridotite. Geochim. Cosmochim. Acta 239, 235–254.
Stagno, V., 2019. Carbon, carbides, carbonates and carbonatitic melts in the Earth's interior. J. Geol. Soc. 176 (2), 375–387.
Stagno, V., Frost, D.J., 2010. Carbon speciation in the asthenosphere: experimental measurements of the redox conditions at which carbonate-bearing melts coexist with graphite or diamond in peridotite assemblages. Earth Planet. Sci. Lett. 300 (1–2), 72–84.
Stagno, V., Frost, D.J., McCammon, C.A., Mohseni, H., Fei, Y., 2015. The oxygen fugacity at which graphite or diamond forms from carbonate-bearing melts in eclogitic rocks. Contrib. Mineral. Petrol. 169 (2), 1–18.
Stagno, V., Stopponi, V., Kono, Y., Manning, C.E., Irifune, T., 2018. Experimental determination of the viscosity of Na_2CO_3 melt between 1.7 and 4.6 GPa at 1200–1700° C: implications for the rheology of carbonatite magmas in the Earth's upper mantle. Chem. Geol. 501, 19–25.
Stagno, V., Kono, Y., Stopponi, V., Masotta, M., Scarlato, P., Manning, C.E., 2020. The viscosity of carbonate- silicate transitional melts at Earth's upper mantle pressures and temperatures, determined by the in situ falling- sphere technique. Carbon Earth's Interior 223–236.
Streckeisen, A., 1974. Classification and nomenclature of plutonic rocks recommendations of the IUGS subcommission on the systematics of igneous rocks. Geol. Rundsch. 63, 773–786.
Taylor, W.R., 1998. An experimental test of some geothermometer and geobaro-meter formulations for upper mantle peridotites with application to the ther-mobarometry of fertile lherzolite and garnet websterite. Neues Jahrb. Mineral. Abhand. 381–408.
Thomson, A.R., Walter, M.J., Kohn, S.C., Brooker, R.A., 2016. Slab melting as a barrier to deep carbon subduction. Nature 529 (7584), 76–79.
Trua, T., Esperança, S., Mazzuoli, R., 1998. The evolution of the lithospheric mantle along the N. African Plate: geochemical and isotopic evidence from tholeiitic and alkaline rocks of the Hyblean Plateau, Italy. Contrib. Mineral. Petrol. 131, 307–322.
Ulmer, P., Luth, R.W., 1991. The graphite-COH fluid equilibrium in P, T, fO_2 space. Contrib. Mineral. Petrol. 106, 265–272.
Warren, J.M., 2016. Global variations in abyssal peridotite compositions. Lithos 248, 193–219.
Woodland, A.B., Koch, M., 2003. Variation in oxygen fugacity with depth in the upper mantle beneath the Kaapvaal craton, Southern Africa. Earth Planet. Sci. Lett. 214 (1–2), 295–310.
Woodland, A.B., Gräf, C., Sandner, T., Höfer, H.E., Seitz, H.M., Pearson, D.G., Kjarsgaard, B.A., 2021. Oxidation state and metasomatism of the lithospheric mantle beneath the Rae Craton, Canada: strong gradients reflect craton formation and evolution. Sci. Rep. 11 (1), 1–10.
Yamamoto, J., Nishimura, K., Sugimoto, T., Takemura, K., Takahata, N., Sano, Y., 2009. Diffusive fractionation of noble gases in mantle with magma channels: origin of low He/Ar in mantle-derived rocks. Earth Planet. Sci. Lett. 280 (1–4), 167–174.
Yaxley, G.M., Crawford, A.J., Green, D.H., 1991. Evidence for carbonatite metasomatism in spinel peridotite xenoliths from western Victoria, Australia. Earth Planet. Sci. Lett. 107 (2), 305–317.
Zhang, C., Duan, Z., 2009. A model for C-O-H fluid in the Earth's mantle. Geochim. Cosmochim. Acta 73 (7), 2089–2102.
Ziberna, L., Klemme, S., Nimis, P., 2013. Garnet and spinel in fertile and depleted mantle: insights from thermodynamic modelling. Contrib. Mineral. Petrol. 166, 411–421.